Materials Advances

ROYAL SOCIETY OF CHEMISTRY

PAPER

View Article Online
View Journal | View Issue

Cite this: *Mater. Adv.*, 2026, 7, 4559

Amine-modified MOF-14 as a tunable platform for CO_2 adsorption and supercapacitor energy storage

Pooja Sharda,[a] Manisha,[b] Anshu Sharma,[c] Miroslav Almáši *[d] and Ankur Jain *[aef]

Received 10th December 2025,
Accepted 19th March 2026

DOI: 10.1039/d5ma01438g

rsc.li/materials-advances

Amine-functionalized copper(II)-based MOF-14 materials were prepared *via* post-synthetic modification using ethylenediamine (en), diethylenetriamine (deta), and 1,2-bis(3-aminopropylamino)ethane (bape) at varying incorporation levels. Comprehensive structural, morphological, textural, and thermal analyses verified the successful grafting of amine functionalities while maintaining the integrity of the parent framework. CO_2 adsorption studies at 0 °C demonstrated that en- and deta-modified MOF-14 exhibited optimal uptake at loadings of 10–15 wt%, achieving a balance between enhanced chemisorption sites and accessible pore volume, whereas the larger bape ligand led to substantial pore obstruction. Additional adsorption measurements at 25 °C confirmed measurable CO_2 uptake under conditions closer to practical gas separation processes. Furthermore, evaluation of CO_2/N_2 separation performance, including IAST calculations for a 15% CO_2/85% N_2 mixture, revealed substantially enhanced selectivity in the amine-modified frameworks compared to pristine MOF-14. Electrochemical evaluation revealed the excellent energy storage performance of MOF-14 (en) 20%, delivering a high specific capacitance of 972 F g^{-1}, markedly outperforming the pristine material. This study highlights the dual capability of amine-modified MOF-14, presenting efficient low-pressure CO_2 capture alongside outstanding promise as an electrode material for high-performance supercapacitors.

1. Introduction

Porous coordination polymers (PCPs), commonly referred to as metal–organic frameworks (MOFs), represent one of the most extensively explored classes of porous materials discovered over the past four decades.[1,2] These crystalline architectures are composed of metal ions or clusters interconnected by organic linkers, forming extended polymeric frameworks with exceptionally high surface areas and tunable pore structures. The ability to tailor their topology, pore size, and chemical functionality makes MOFs suitable for a broad range of applications, including gas storage and separation,[3–5] heterogeneous catalysis,[6,7] drug delivery,[8–10] sensing,[11,12] ion exchange,[13,14] environmental remediation,[15–18] and energy storage.[19–21]

Among the mentioned applications, gas adsorption, particularly carbon dioxide capture, remains a primary focus due to its environmental significance.[22] Anthropogenic CO_2 emissions from fossil fuel combustion, industrial processes, and transportation are a major driver of global warming and climate change.[19] The development of efficient CO_2 capture and storage technologies is therefore essential for mitigating greenhouse gas emissions. MOFs offer significant potential in this regard, owing to their tunable porosity, high density of adsorption sites, and structural versatility. For example, MOF-74 (Mg_2(dobpdc)) exhibits low-pressure CO_2 uptake (up to 30.1 wt%), while NU-111 demonstrates high-pressure storage capacities of up to 61.8 wt%.[23]

A widely employed strategy to enhance CO_2 affinity involves incorporating nitrogen-containing or amine functionalities into the MOF structure, either through direct synthesis or post-synthetic modification. Such functionalization promotes chemisorptive interactions with CO_2 at low temperatures, facilitating efficient adsorption–desorption cycles.[24–27] Notably,

[a] *Centre for Renewable Energy & Storage, Suresh Gyan Vihar University, Jaipur 302017, India. E-mail: ankur.j.ankur@gmail.com*
[b] *Department of Physics and Astrophysics, School of Basic Sciences, Central University of Haryana, Mahendragarh 123031, India*
[c] *Department of Applied Sciences and Humanities, School of Engineering & Technology, Central University of Haryana, Mahendragarh 123031, India*
[d] *Department of Inorganic Chemistry, Faculty of Science, P. J. Safarik University, Moyzesova 11, Kosice 041 54, Slovak Republic. E-mail: miroslav.almasi@upjs.sk*
[e] *Natural Science Centre for Basic Research & Development, Hiroshima University, Higashi-Hiroshima 739-8530, Japan*
[f] *Institute for Catalysis and Energy Solutions, College of Science, Engineering and Technology, University of South Africa, Private Bag X6, Florida 1710, South Africa*

tetraamine-appended MOF-74 has achieved CO_2 storage capacities of up to 90 wt%.[28,29] The choice of organic linker is also critical, as its geometry, length, and functional groups dictate framework topology, pore dimensions, and chemical environment.[30,31] Polar functional groups and open metal sites enhance CO_2 binding, while extended aromatic linkers can modulate framework flexibility and adsorption selectivity.[32–35]

For practical CO_2 capture, several key parameters must be optimized: adsorption capacity, thermal and chemical stability, regeneration efficiency, and cost-effective synthesis.[36,37] High thermal stability is essential for repeated adsorption–desorption cycles, and structural robustness ensures long-term operational durability.[38,39] Recent research efforts have increasingly focused on multifunctional MOFs that combine high gas adsorption performance with other advanced properties, such as electrochemical activity.[40,41] For instance, Bhosale *et al.* developed a porous nanorod-based Ni-MOF which delivered a specific capacitance of 1956.3 F g^{-1} at a current density of 5 mA cm^{-2}.[42] Krishnan *et al.* synthesized Cu-MOF and decorated it with reduced graphene oxide to achieve a specific capacitance of 867.09 F g^{-1}.[43] Similarly, Khan *et al.* fabricated amine-functionalized Cd-based MOF and utilized it for energy storage applications and obtained a specific capacitance of 9.8 mF cm^{-2}. The performance was further enhanced by synthesizing its composite with reduced graphene oxide (rGO) and multi-walled carbon nanotubes (MWCNTs).[44] These studies clearly demonstrate that MOFs, owing to their tunable structure and high specific surface area, with some modifications, offer promising potential for energy storage applications.

MOF-14, with the chemical formula $[Cu_3(BTB)_2(H_2O)(DMF)_5]\cdot 4DMF\cdot 2H_2O$ (BTB = 1,3,5-benzenetribenzoate), is a copper(II)-based coordination framework constructed from dinuclear Cu_2 paddle-wheel secondary building units (SBUs) (Fig. 1a) connected by trigonal BTB linkers coordinated in *syn–syn* fashion (Fig. 1b).[45] Each BTB linker coordinates to three Cu_2 clusters, while each cluster is connected to four BTB ligands, generating an augmented (3,4)-connected net with Pt_3O_4 topology (Fig. 1c). The resulting structure consists of two identical, interwoven but non-intersecting frameworks. This interpenetrated architecture forms a three-dimensional network of large, accessible cavities (~16.4 Å in diameter) interconnected by apertures of approximately 7.7 × 14.0 Å. In the as-synthesized material, these cavities host axially bound water molecules, DMF ligands coordinated to Cu(II) sites, and additional solvent guests, which collectively occupy about two-thirds of the unit cell volume. Removal of these guests exposes coordinatively unsaturated Cu(II) sites (CUSs, Fig. 1d), which act as strong Lewis acid centres. These sites readily interact with Lewis bases such as amines, enabling targeted post-synthetic modification. Such functionalization can enhance CO_2 capture *via* acid–base interactions and introduce additional redox-active sites, improving electrochemical performance in supercapacitor applications.

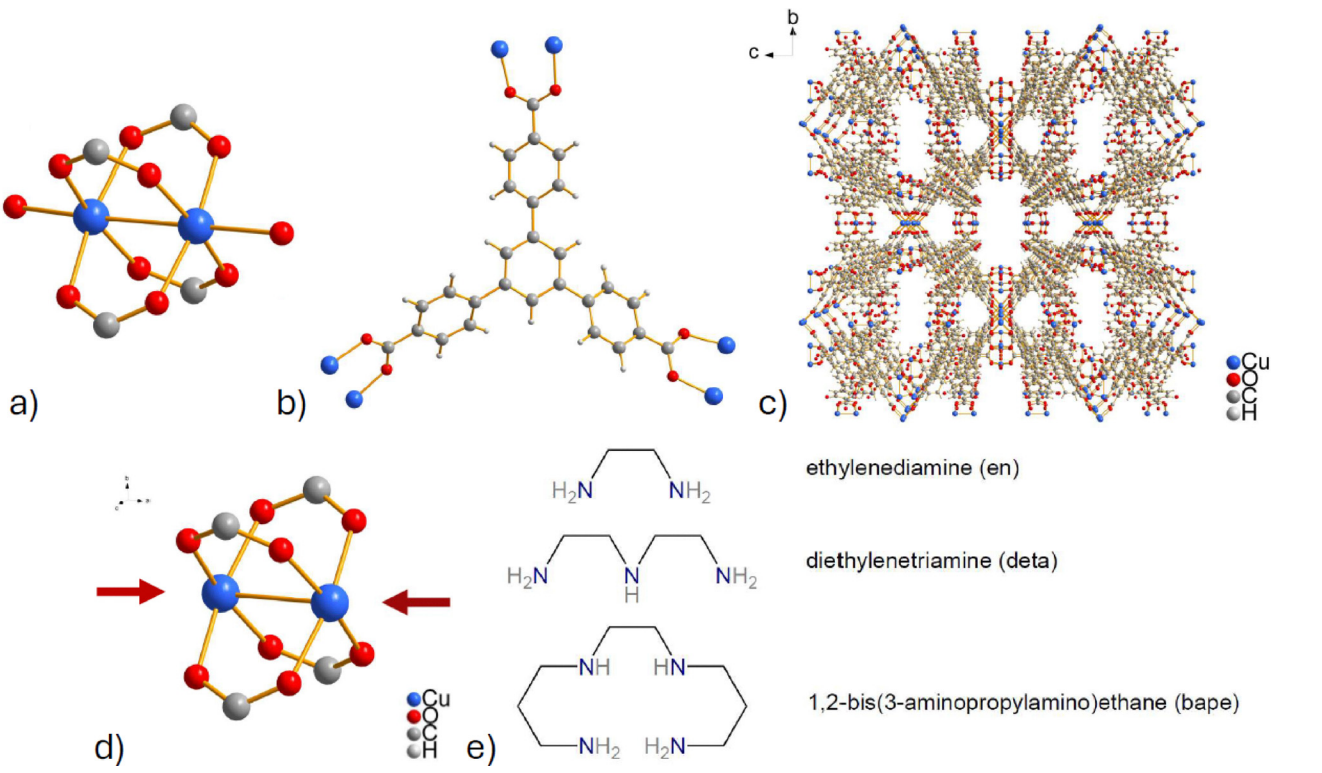

Fig. 1 Structural representation of MOF-14: (a) secondary building unit (SBU) consisting of a Cu_2 paddle-wheel cluster; (b) 1,3,5-benzenetribenzoate (BTB) organic linker showing the coordination mode of the carboxylate groups; (c) extended three-dimensional framework of MOF-14 with Pt_3O_4 topology viewed along the *a*-axis. (d) Paddle-wheel cluster in MOF-14 with coordinatively unsaturated sites (CUSs, red arrows) for binding of amines, and (e) molecular structure of amines used in the post-synthetic modification.

In our previous study, we investigated the post-synthetic modification of HKUST-1 with diamine and triamine linkers, demonstrating that such functionalization significantly enhanced its performance in hydrogen and CO_2 storage applications.[46] Building on these findings, the present work aimed to expand the linker structure of HKUST-1 by replacing 1,3,5-benzenetricarboxylate (BTC) with the elongated 1,3,5-benzenetribenzoate (BTB) linker, thereby constructing the MOF-14 framework. Both compounds share the characteristic binuclear Cu_2 paddle-wheel secondary building unit and a tricarboxylate-based linker. However, in MOF-14, the BTC linker is expanded by additional phenyl rings, resulting in a larger pore system and enhanced structural complexity. In addition to diamine and triamine modifiers, a tetraamine was also employed, and the resulting materials were evaluated for CO_2 adsorption performance as well as electrochemical properties relevant to supercapacitor applications.

In this work, a rapid, high-yield synthesis of MOF-14 under mild conditions, followed by post-synthetic modification with three polyamines: ethylenediamine (en), diethylenetriamine (deta), and 1,2-bis(3-aminopropylamino)ethane (bape) (Fig. 1e), at various loadings was investigated. The structural, thermal, morphological, textural, and electrochemical properties of pristine and amine-functionalized MOF-14 were systematically investigated. Despite extensive research on MOF based materials, most studies focus either on gas adsorption or electrochemical energy storage independently, often relying on carbonization or heavy composite formation that compromises structural integrity. Herein, our particular emphasis was placed on correlating amine loading with CO_2 adsorption performance and supercapacitor behaviour, with the aim of identifying optimal modification conditions for multifunctional applications.

2. Experimental details

2.1 Chemicals

All chemicals used for the synthesis, solvent exchange, and post-synthetic modification of MOF-14 were purchased from Sigma-Aldrich (analytical grade) and used without further purification. The reagents included 1,3,5-benzenetribenzoic acid (H_3BTB, $\geq$98%), copper(II) nitrate hemipentahydrate ($Cu(NO_3)_2{\cdot}2.5H_2O$, $\geq$99%), *N*,*N*′-dimethylformamide (DMF, $\geq$99.8%), pyridine ($\geq$99%), ethanol (EtOH, $\geq$99%), methanol (MeOH, $\geq$99.8%), ethylenediamine (en, $\geq$99%), diethylenetriamine (deta, 99%), and 1,2-bis(3-aminopropylamino)ethane (bape, 96%).

2.2 Synthesis of MOF-14 and solvent exchange

The as-synthesized MOF-14 (AS), with the formula $[Cu_3(BTB)_2(H_2O)(DMF)_5]{\cdot}4DMF{\cdot}2H_2O$, was prepared according to the following procedure.[46] 1,3,5-Benzenetribenzoic acid (H_3BTB, 0.023 g, 0.052 mmol) and copper(II) nitrate hemipentahydrate ($Cu(NO_3)_2{\cdot}2.5H_2O$, 0.065 g, 0.28 mmol) were dissolved in a mixed solvent of ethanol (3 mL), *N*,*N*′-dimethylformamide (DMF, 3 mL), and deionized water (2 mL), in the presence of excess pyridine (0.62 mmol). The reaction mixture was maintained at 65 °C for 24 h, affording light-blue, needle-shaped crystals of MOF-14. The product was air-stable and insoluble in water as well as in common organic solvents. The synthesis was repeated in multiple batches until approximately 4 g of MOF-14 (AS) was obtained, sufficient for solvent exchange, post-synthetic modification, and characterization.

For activation, coordinated and pore-occluded DMF molecules (b.p. 153 °C) in MOF-14 (AS) were replaced with methanol (b.p. 65 °C) to facilitate solvent removal at lower temperatures. The solvent exchange was carried out in a Soxhlet apparatus for 48 h, using methanol as the extracting solvent, yielding the exchanged form, MOF-14 (EX). Subsequent activation afforded MOF-14 (AC).

2.3 Post-synthetic amine modification

Activated MOF-14 (AC) (100 mg; activation conditions: 100 °C, 30 min, oven-dried) was dispersed in 5 mL of anhydrous methanol under a nitrogen atmosphere. The desired amine, ethylenediamine (en), diethylenetriamine (deta), or 1,2-bis(3-aminopropylamino)ethane (bape) (Fig. 1e), was added in the required amount to achieve target mass fractions of 5, 10, 15, 20, or 30 wt% relative to MOF-14. Anhydrous methanol was then added to adjust the total volume of the suspension to 10 mL. The reaction mixtures were stirred for 24 h under an inert atmosphere. The resulting amine-modified MOF-14 materials were collected by filtration, washed repeatedly with methanol, and dried before further characterization. For ethylenediamine, all intended loadings (5–30 wt%) were successfully obtained. In contrast, for deta and bape, structural degradation of MOF-14 occurred at loadings of 20 and 30 wt%, and therefore only samples containing 5, 10, and 15 wt% amine were successfully prepared (see Fig. S1 in SI).

2.4 Characterization

Fourier-transform infrared (FTIR) spectra were recorded at ambient laboratory temperature on a Thermo Scientific Avatar FT-IR 6700 spectrometer equipped with an ATR accessory, in the wavenumber range of 4000–400 cm^{-1}, and a resolution of 2 cm^{-1} with 128 repetitions.

Powder X-ray diffraction (PXRD) patterns were recorded on a Bruker D2 diffractometer using Cu Kα radiation (λ = 1.5406 Å) in Bragg–Brentano geometry over the 2θ range of 2–40° at a scan rate of 0.5° min^{-1} to confirm the crystalline structure and phase purity of the samples.

Thermal stability, dehydration behaviour, and the amount of grafted amine were determined by thermogravimetric analysis (TGA) using a Hitachi DSC7020 analyzer. The samples were heated from 25 °C to 850 °C under a continuous air flow.

The morphology and elemental composition were examined using a Nova NanoSEM 450 field-emission scanning electron microscope (FEI) equipped with an energy-dispersive X-ray spectroscopy (EDS) detector, operated at an accelerating voltage of 15 kV.

Nitrogen (N_2) and carbon dioxide (CO_2) adsorption/desorption isotherms were measured using a NovaTouch LX4 surface area and pore size analyzer (Quantachrome, Anton Paar, 2021) after degassing the samples at 100 °C for 24 h.

Electrochemical properties were evaluated using a BioLogic VSP-300 electrochemical workstation by cyclic voltammetry (CV), galvanostatic charge–discharge (GCD), and electrochemical impedance spectroscopy (EIS) measurements to assess the energy storage capabilities of the synthesized materials.

3. Results and discussion

3.1 Synthesis, postsynthetic modification and powder X-ray diffraction

The copper(II)-based MOF-14 with the formula $[Cu_3(BTB)_2(H_2O)(DMF)_5]\cdot 4DMF\cdot 2H_2O$ was synthesized by solvothermal reaction of 1,3,5-benzenetribenzoic acid (H_3BTB) and $Cu(NO_3)_2\cdot 2.5H_2O$ in a mixture of DMF, ethanol, and water in the presence of excess pyridine. The as-synthesized product (MOF-14 (AS)) was further subjected to solvent exchange using methanol to afford the methanol-exchanged sample (MOF-14 (EX)), and subsequent thermal treatment yielded the activated material (MOF-14 (AC)).

The phase purity and crystallinity of MOF-14 were evaluated by powder X-ray diffraction (PXRD) for the AS, EX, and AC samples. The experimental PXRD patterns closely match the simulated powder diffraction pattern generated from the reported single-crystal crystallographic data (see Fig. S2a in SI),[47] confirming successful formation of the target MOF-14 structure. Importantly, all major reflections remain at identical 2θ positions after solvent exchange and thermal activation, demonstrating that the framework topology is preserved throughout the treatment steps.

Upon thermal activation, the coordinated water molecules at the axial positions of the Cu_2 paddle-wheel clusters were removed, generating coordinatively unsaturated Cu(II) sites (CUSs, Fig. 1d). These open metal sites (OMSs) act as strong Lewis acid centres capable of binding Lewis basic amine molecules through metal–nitrogen coordination. Owing to the relatively large pore apertures (7.7 × 14.0 Å) and spacious internal cavities (16.4 × 16.4 Å) of MOF-14, all three employed polyamines: ethylenediamine (en), diethylenetriamine (deta), and 1,2-bis(3-aminopropylamino)ethane (bape) (Fig. 1e), can access the framework interior and coordinate directly to the CUSs, enabling uniform functionalization throughout the material.

Post-synthetic amine modification of MOF-14 (AC) was carried out using polyamine molecules: en, deta, and bape, at various weight loadings (5, 10, 15, 20, and 30 wt%). While the modification with ethylenediamine was successful across the full mass fraction range, the use of deta and bape resulted in structural degradation at higher amine loadings (20 and 30 wt%), likely due to excessive interaction of the bulky amines with the framework. Therefore, only samples with 5, 10, and 15 wt% content of deta and bape were retained for further analysis.

PXRD patterns of all amine-functionalized samples, en-, deta-, and bape-modified series at the investigated loadings, are provided in Fig. S2b, c and d, respectively. The characteristic diffraction peaks of MOF-14 remain at identical 2θ positions after post-synthetic amine treatment, confirming preservation of the crystalline framework. Minor variations in relative peak intensities are attributed to partial pore occupation, changes in electron density upon amine coordination to the open Cu(II) sites, and possible preferred orientation of anisotropic crystallites during PXRD sample preparation. In contrast, samples prepared with higher loadings of deta and bape (20–30 wt%) exhibit complete disappearance of characteristic Bragg reflections and display a broad halo-type diffraction profile, indicating full amorphization of the MOF-14 framework.

The synthesized MOF-14 and amine-functionalized derivatives were characterized by infrared spectroscopy (IR), thermogravimetric analysis (TG), scanning electron microscopy (SEM), and nitrogen adsorption measurements to evaluate their thermal stability, structural integrity, and textural properties.

3.2 Infrared spectroscopy

Infrared (IR) spectroscopy was employed to verify the formation of the MOF-14 framework and to monitor structural changes during solvent exchange and thermal activation. The spectra of MOF-14 (AS), MOF-14 (EX), and MOF-14 (AC) depicted in Fig. S3 in SI were recorded in the range of 4000–400 cm^{-1}, and selected absorption bands are summarized in Table 1. All three materials exhibit prominent bands characteristic of metal–carboxylate coordination. The asymmetric ($\nu(COO^-)_{as}$) and symmetric ($\nu(COO^-)_s$) stretching vibrations of the coordinated carboxylate groups are observed in the regions 1605–1598 cm^{-1} and 1385–1398 cm^{-1}, respectively. The position of these bands confirms successful coordination between Cu(II) ions and the carboxylate moieties of the 1,3,5-benzenetribenzoate (BTB) linker. Bands observed in the 1546–1525 cm^{-1} region are assigned to aromatic C=C skeletal vibrations ($\nu(C{=}C)_{ar}$), which support the incorporation of the benzene-based linker into the MOF framework. Additionally, a medium-intensity band appearing around 776–779 cm^{-1} is attributed to the bending vibration of the carboxylate group ($\delta(COO^-)$), commonly arising from out-of-plane deformation modes. The presence of all these framework-related bands across all samples confirms the integrity of the MOF-14 throughout the solvent exchange and activation processing. In the as-synthesized material (MOF-14 (AS)), a broad absorption band at 3441 cm^{-1} is observed, corresponding to O–H stretching vibrations from both coordinated water molecules and physisorbed moisture within the pores. Two bands at 2926 and 2860 cm^{-1} are attributed to aliphatic C–H stretching vibrations of DMF (*N*,*N*′-dimethylformamide), while the intense band at 1660 cm^{-1} is assigned to the C=O stretching vibration of DMF molecules. Following solvent exchange with methanol (MOF-14 (EX)), the O–H stretching band shifts to 3404 cm^{-1} and becomes broader, indicating the presence of

Table 1 Selected infrared absorption bands (in cm^{-1}) observed for MOF-14 materials in different stages (as-synthesized, solvent-exchanged, activated) and after post-synthetic amine modification with ethylenediamine (en), diethylenetriamine (deta), and 1,2-bis(3-aminopropylamino)ethane (bape)

	ν(OH)	ν(NH)	$\nu(CH)_{aliph}$	ν(C=O)	δ(NH)	$\nu_{as}(COO^-)$	$\nu_s(COO^-)$	$\delta(COO^-)$
MOF-14(AS)	3441	—	2926 2860	1660	—	1605	1385	779
MOF-14 (EX)	3404	—	2977 2940 2831	—	—	1601	1389	779
MOF-14 (AC)	—	—	—	—	—	1598	1398	776
MOF-14 (en) 5%	—	3243 3142	2948 2891	—	1581	1529	1374	772
MOF-14 (en) 10%	—	3243 3143	2948 2889	—	1580	1531	1373	774
MOF-14 (en) 15%	—	3243 3142	2947 2889	—	1580	1531	1369	777
MOF-14 (en) 20%	—	3241 3142	2946 2891	—	1579	1530	1366	777
MOF-14 (en) 30%	—	3242 3140	2947 2890	—	1579	1530	1365	778
MOF-14 (deta) 5%	—	3320 3234 3145	2933 2880	—	1580	1532	1372	773
MOF-14 (deta) 10%	—	3320 3235 3145	2933 2879	—	1581	1537	1370	779
MOF-14 (deta) 15%	—	3322 3233 3147	2935 2881	—	1579	1536	1368	778
MOF-14 (bape) 5%	—	3367 3289 3235 3143	2952 2928 2878	—	1586	1544	1369	781
MOF-14 (bape) 10%	—	3365 3286 3238 3142	2955 2928 2878	—	1585	1543	1365	780
MOF-14 (bape) 15%	—	3369 3289 3237 3142	2953 2928 2878	—	1585	1543	1366	780

hydrogen-bonded methanol within the pore system. Multiple C–H aliphatic stretching bands at 2977, 2940, and 2831 cm^{-1} are observed, which are characteristic of methanol. Importantly, the DMF-related C=O stretching band at 1660 cm^{-1} disappears, confirming its successful removal and replacement by methanol molecules. In the activated sample (MOF-14 (AC)), no O–H or aliphatic C–H stretching bands are observed, indicating complete removal of residual solvent molecules. The framework-specific bands remain unchanged, with only minor shifts in the carboxylate vibrational modes, suggesting a slight change in the coordination environment but preservation of the MOF structure.

After activation, MOF-14 was post-synthetically modified with various polyamine ligands, ethylenediamine (en), diethylenetriamine (deta), and 1,2-bis(3-aminopropylamino)ethane (bape), in mass fractions ranging from 5 to 30 wt%. The incorporation of these amines was confirmed by IR spectroscopy through the emergence of new vibrational bands not present in the unmodified framework (see Fig. 2 and Table 1). All amine-modified materials exhibited intense and well-defined bands in the region 3300–3100 cm^{-1}, corresponding to N–H stretching vibrations. In the case of MOF-14 (en) samples, two distinct bands at ~3243 and 3142 cm^{-1} are consistent with symmetric and asymmetric stretching modes of primary amine groups. For MOF-14 (deta) materials, three separate N–H stretching bands appear at ~3320, 3234, and 3145 cm^{-1}, reflecting the presence of both primary and secondary amine functionalities in the molecule. The IR spectra of bape-modified MOF-14 show four N–H stretching bands between 3367 and 3143 cm^{-1}, which can be attributed to its extended structure with multiple terminal and internal amino groups. The increased complexity and intensity of N–H bands in the bape series correlate with the higher number of donor sites per molecule. The presence of aliphatic C–H stretching vibrations in the range 2955–2878 cm^{-1} further supports the successful encapsulation or grafting of alkylamine chains within the MOF-14. Additionally, all amine-functionalized samples display a band in the range 1580–1586 cm^{-1}, assigned to N–H bending vibrations (δ(NH)). At the same time, small but consistent shifts are observed in the carboxylate vibrational modes when compared to the activated MOF-14. Specifically, the $\nu_{as}(COO^-)$ and $\nu_s(COO^-)$ bands are shifted to 1579–1586 cm^{-1} and 1365–1374 cm^{-1}, respectively, while the bending mode $\delta(COO^-)$ appears at 772–781 cm^{-1}. These shifts are attributed to weak interactions between the amine groups and the MOF structure, most likely *via* hydrogen bonding or electrostatic effects involving the carboxylate functionalities or the open Cu(II) coordination sites. The extent of these shifts correlates modestly with the number of amino groups and the molecular structure of the grafted amine. Importantly, no new bands indicative of degradation or structural decomposition were observed, confirming that the framework remained intact during post-synthetic modification.

3.3 Thermogravimetric analysis

All materials were characterized by thermogravimetric analysis (TG) combined with differential thermal analysis (DTA). The measurements were performed in an air atmosphere over the temperature range of 25–850 °C, and the obtained TG and DTA curves for MOF-14 are presented in Fig. S4 in SI, and for amine-modified materials in Fig. 3. Based on these measurements, the thermal stability of the samples was evaluated, and the amount of grafted amines was determined. To eliminate the contribution of adsorbed and weakly bound solvents, all TG curves were normalized to the sample mass at 150 °C.[48,49] The corresponding weight losses were then distributed between the mass change of the organic framework and the residual mass after complete combustion. This normalization allowed for a more precise calculation of the amount of grafted amines.

For the methanol-exchanged MOF-14 sample, the TG curve (see Fig. S4 in SI) shows an initial weight loss of 13.8% in the temperature range of 25–150 °C, which is attributed to the removal of solvents (water and methanol). This desolvation step is accompanied by an endothermic effect on the DTA curve with a peak at 68 °C. The material remains stable up to 280 °C, after which a major weight loss occurs between 280 and 500 °C due to the decomposition of the BTB linker (organic part of the framework). This process is associated with two distinct exothermic peaks on the DTA curve at 318 and 352 °C.

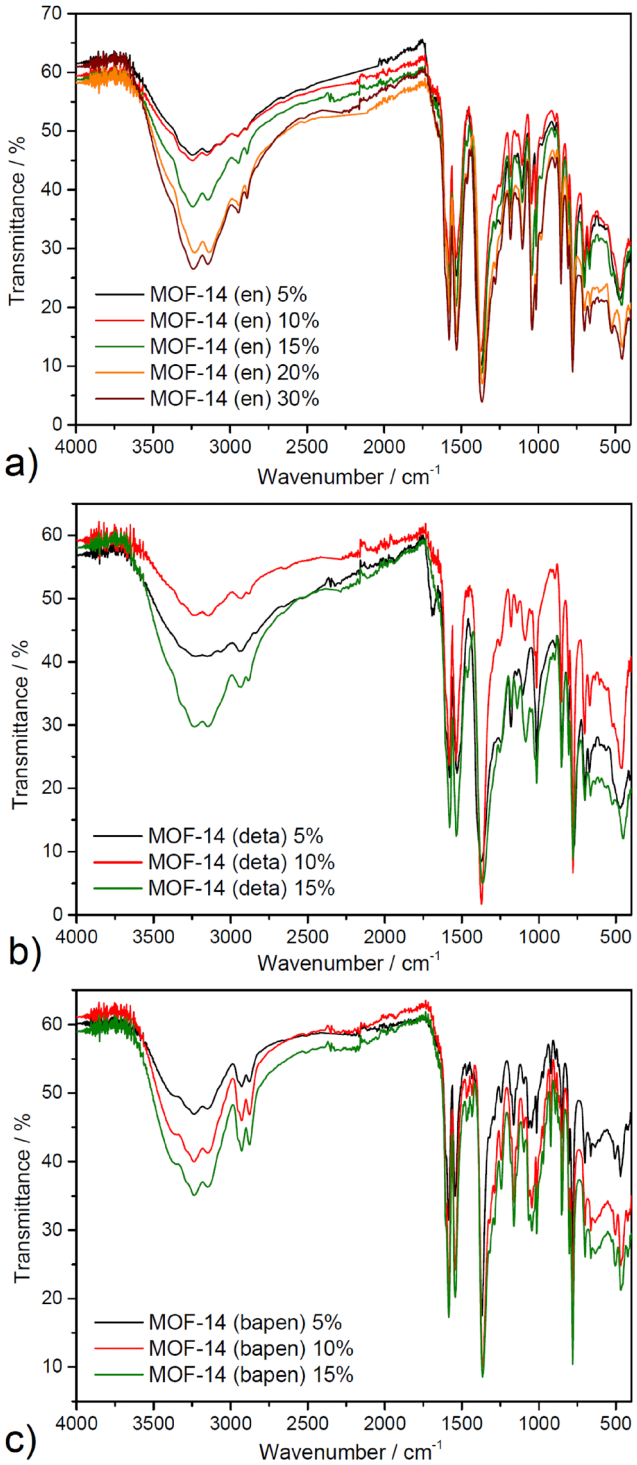

Fig. 2 IR spectra of amine-modified MOF-14 with (a) ethylenediamine (en), (b) diethylenetriamine (deta), and (c) 1,2-bis(3-aminopropylamino)-ethane (bape) with different mass fractions.

The TG, normalized TG, and DTA curves for all amine-modified MOF-14 samples are presented in Fig. 3. Based on the residual masses, the amount of grafted amines was calculated in both mg g^{-1} and mmol g^{-1}, and the results are summarized in Table 2. On the TG curves of the amine-modified samples, the first step corresponds to the removal of solvent molecules, with weight losses ranging from 9.5–17.9% for en-modified, 9.0–12.1% for deta-modified, and 11.8–12.9% for bape-modified materials, occurring in the temperature range of 25–150 °C. The dehydration/desolvation step was accompanied by endothermic effects on the DTA curves, observed at 54–60 °C for en, 50–62 °C for deta, and 52–60 °C for bape-modified materials. In the second step of thermal decomposition, the release of grafted amines was observed, manifested by endothermic effects on the DTA curves. For ethylenediamine-modified samples, three endothermic peaks were detected in the temperature range of 211–316 °C, while diethylenetriamine-modified samples exhibited a single endothermic effect within 252–293 °C, and 1,2-bis(3-aminopropylamino)ethane-modified samples displayed two endothermic peaks in the range of 253–264 °C. Further increase in temperature leads to the decomposition of the polymeric framework of MOF-14, accompanied by major weight loss, characteristic of the oxidative degradation of the BTB linker. From the normalized TG curves, the amounts of grafted amines were calculated based on the difference in residual masses between the pristine MOF-14 and the amine-modified materials.

The calculated amounts of grafted amines (see Table 2) reflect the influence of both the type of amine and its nominal loading during the modification process. For the en-modified samples, the amine content increases significantly from 82.3 mg g^{-1} (1.371 mmol g^{-1}) at 5% loading to 178.1–178.7 mg g^{-1} ($\approx$2.97–2.98 mmol g^{-1}) at 10–15% loading, followed by a slight decrease at 20% loading (177.0 mg g^{-1}; 2.950 mmol g^{-1}) and a subsequent increase to 200.8 mg g^{-1} (3.346 mmol g^{-1}) at 30% loading. This trend suggests that, above a certain concentration, the grafting efficiency approaches saturation, with additional amine incorporation being limited by steric hindrance or pore blocking effects. In the case of deta-modified materials, the grafted amounts are consistently higher compared to the en-series at the same nominal loadings, starting from 165.4 mg g^{-1} (1.603 mmol g^{-1}) at 5% loading and reaching 224.8 mg g^{-1} (2.179 mmol g^{-1}) at 15% loading. The higher mass values for deta compared to en at low loadings can be attributed to the larger molecular weight of deta, even though the molar amounts remain lower. The bape-modified samples exhibit the highest grafted amounts in terms of mass, ranging from 329.8 to 341.5 mg g^{-1}, which is expected given the much higher molecular weight of bape. However, the molar quantities remain relatively low (1.892–1.959 mmol g^{-1}), indicating that, although more mass is incorporated, the number of grafted molecules is smaller due to the bulky structure of bape, which can also lead to partial pore blocking.

3.4 SEM with EDX

The morphology of pristine and amine-modified MOF-14 samples was examined by field-emission SEM equipped with EDX. The methanol-exchanged MOF-14 shows elongated prismatic/rod-like crystals with smooth faces and well-defined edges, typical for MOF-14, and a relatively narrow size dispersion (see Fig. 4). After ethylenediamine (en) modification,

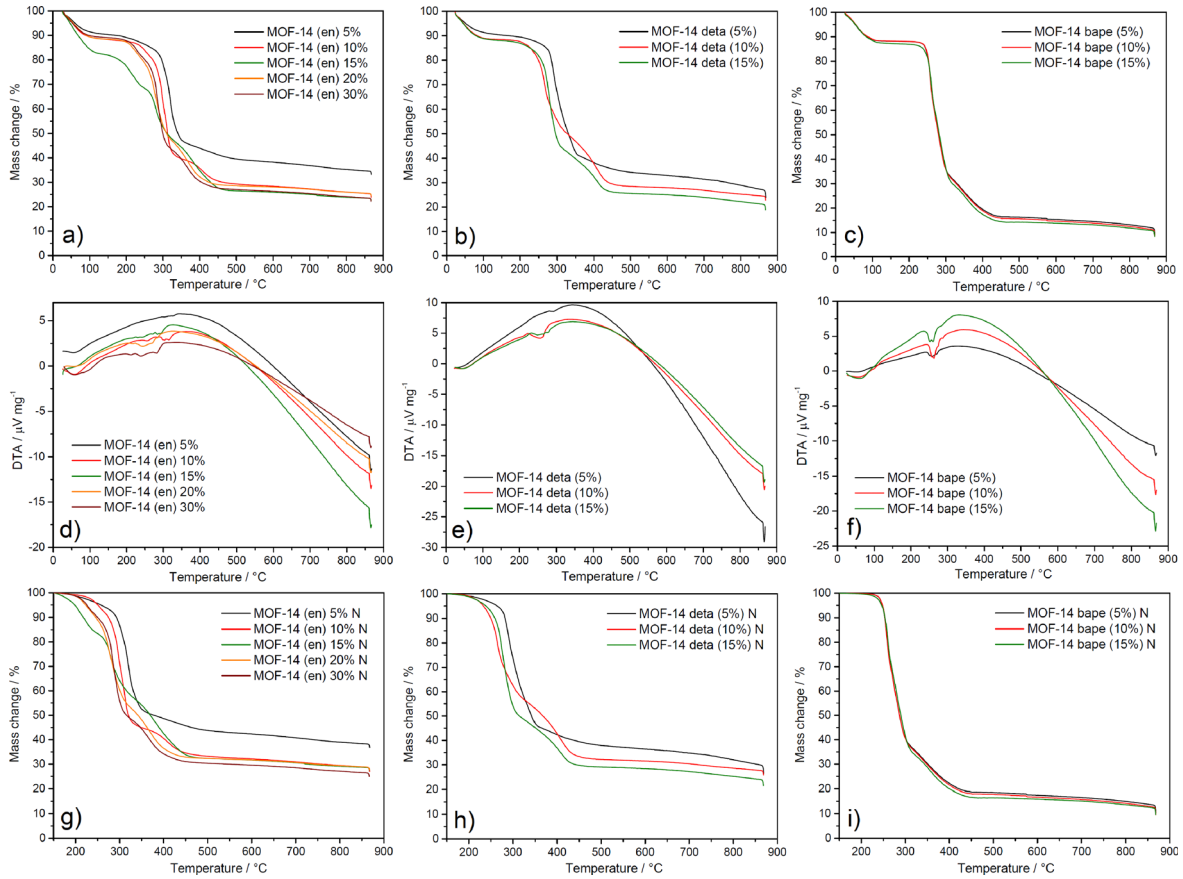

Fig. 3 Thermogravimetric (TG), differential thermal analysis (DTA), and normalized TG curves of MOF-14 samples functionalized with different amounts of (a), (d) and (g) ethylenediamine (en), (b), (e) and (h) diethylenetriamine (deta), and (c), (f) and (i) 1,2-bis(3-aminopropylamino)ethane (bape).

Table 2 Calculated amount of grafted amines (mg g^{-1} and mmol g^{-1}) determined from normalized TG curves

	Amount of amine	
Sample	mg g^{-1}	mmol g^{-1}
MOF-14 (en) 5%	82.3	1.371
MOF-14 (en) 10%	178.1	2.968
MOF-14 (en) 15%	178.7	2.978
MOF-14 (en) 20%	177.0	2.950
MOF-14 (en) 30%	200.8	3.346
MOF-14 (deta) 5%	165.4	1.603
MOF-14 (deta) 10%	188.0	1.822
MOF-14 (deta) 15%	224.8	2.179
MOF-14 (bape) 5%	329.8	1.892
MOF-14 (bape) 10%	337.8	1.938
MOF-14 (bape) 15%	341.5	1.959

progressive surface roughening and fragmentation are observed: at 5 wt% the parent morphology is still discernible but the crystal surfaces become textured; at 10–15 wt% the particles lose their regular prismatic shape and form irregular agglomerates; at 20–30 wt% dense aggregates with poorly defined boundaries dominate, consistent with extensive surface coverage and interparticle adhesion *via* hydrogen-bonding among amine groups. The deta series preserves more of the parent shape at 5 wt% but shows marked roughening and plate-like fragments by 10–15 wt%, indicating partial collapse of outer layers under bulkier triamine grafting. The bape series exhibits the strongest distortion already at 5 wt% (rounded edges, fused aggregates), and at 10–15 wt%, the micrographs are dominated by irregularly coalesced particles suggestive of pore blocking and extensive surface coating by the bulky tetraamine.

Elemental analysis by EDX on a representative highly loaded sample (MOF-14 (en) 30%) confirms the presence of C, Cu, O and N; a standardless quantification yielded approximately C ∼ 42 wt%, Cu ∼ 20 wt%, O ∼ 3.5 wt% and N ∼ 2.4 wt% (see inset table in Fig. S5 in SI). The detection of nitrogen is consistent with successful ethylendiamine incorporation, while copper from the paddle-wheel clusters and oxygen from carboxylates remain prominent, as expected for the MOF-14 framework.

3.5 Nitrogen adsorption/desorption measurements

All samples, including MOF-14 and its amine-functionalized derivatives, were characterized by nitrogen adsorption/desorption measurements at −196 °C. These analyses enabled the determination of Brunauer–Emmett–Teller surface areas (S_{BET}), the results of which are summarized in Table 3 and

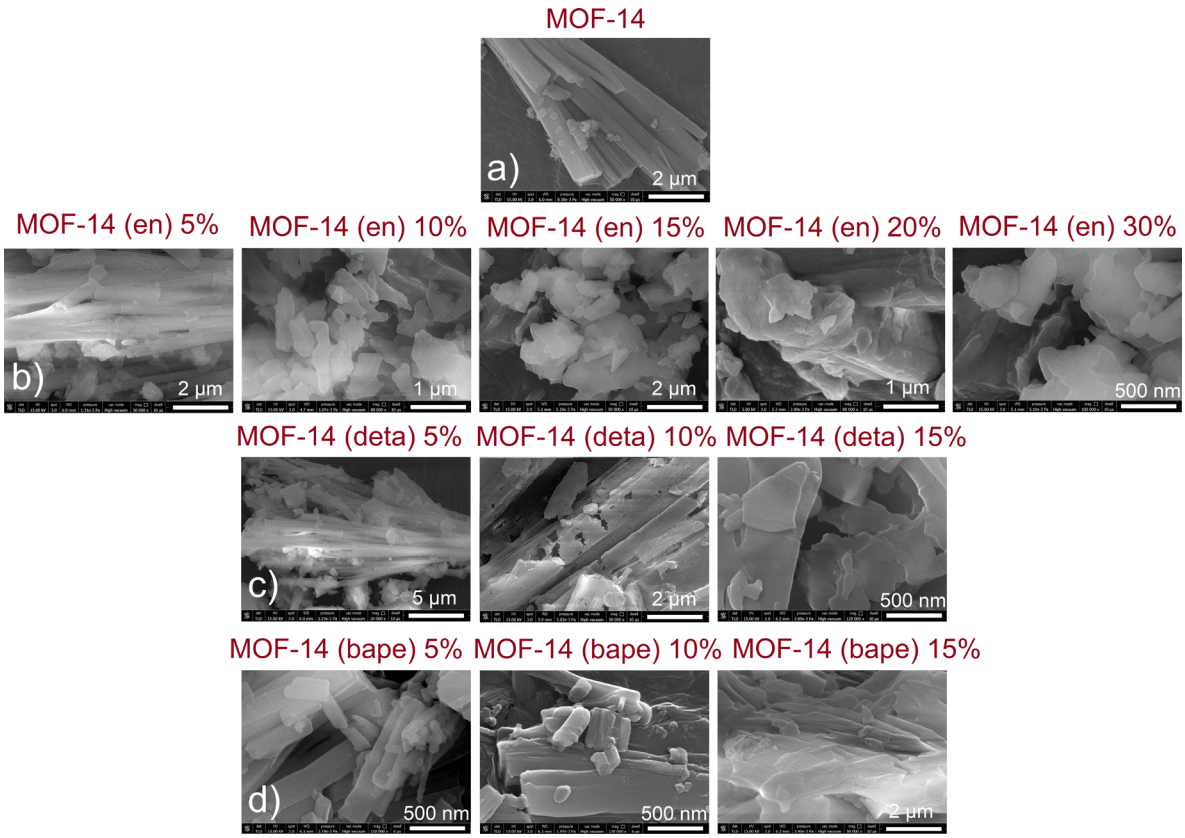

Fig. 4 SEM images of (a) pristine MOF-14 and MOF-14 modified with (b) ethylenediamine (en), (c) diethylenetriamine (deta), and (d) 1,2-bis(3-aminopropylamino)ethane (bape) at the indicated mass fractions.

Table 3 Textural properties (S_{BET}) and CO_2 adsorption capacities@0 °C and 101 325 Pa of pristine and amine-functionalized MOF-14 samples

Sample	S_{BET} ($m^2\ g^{-1}$)	$V(CO_2)$ ($cm^3\ g^{-1}$)	$n(CO_2)$ (mmol g^{-1})	$w(CO_2)$ (wt%)	$V(CO_2)$ ($cm^3\ m^{-2}$)
MOF-14 (AC)	1815.0	129.7	5.79	25.47	0.07
MOF-14 (en) 5%	10.8	31.8	1.42	6.24	2.94
MOF-14 (en) 10%	8.9	61.2	2.73	12.02	6.88
MOF-14 (en) 15%	5.9	53.7	2.40	10.54	9.10
MOF-14 (en) 20%	5.1	45.6	2.03	8.95	8.94
MOF-14 (en) 30%	4.1	43.1	1.92	8.46	10.51
MOF-14 (deta) 5%	14.3	57.5	2.57	11.29	4.02
MOF-14 (deta) 10%	6.1	57.2	2.55	11.23	9.38
MOF-14 (deta) 15%	8.3	58.6	2.61	11.51	7.06
MOF-14 (bape) 5%	6.1	50.9	2.27	9.99	8.34
MOF-14 (bape) 10%	4.2	43.4	1.94	8.52	10.33
MOF-14 (bape) 15%	3.7	35.1	1.57	6.89	9.49

Fig. 5. All materials were activated under vacuum at 100 °C prior to measurement. For MOF-14, a preceding methanol exchange step (MOF-14 (EX)) facilitated the removal of high-boiling DMF from the pores, allowing complete activation at this relatively low temperature. The choice of a mild activation temperature was deliberate, aiming to prevent framework degradation and to avoid the release of coordinated amines from the pores in functionalized samples.

The N_2 adsorption/desorption isotherm of activated MOF-14 (AC) (Fig. S6 in SI) exhibits a steep uptake at very low relative pressures ($p/p_0 < 0.05$) followed by an early plateau, characteristic of a microporous material. According to the IUPAC classification,[50] the profile corresponds to type *I*(*b*), indicative of networks with predominantly narrow-to-wide micropores (≈0.7–2 nm), consistent with the ~1.1 nm apertures and ~1.6 nm cavities of MOF-14. The loop between adsorption and desorption branches at higher p/p_0 is minimal. A slight deviation at $p/p_0 \gtrsim 0.5$ can be ascribed to inter-particle condensation/voids (H4-like artefact) rather than intrinsic mesoporosity, in line with the rigid framework. The BET surface area determined under the BET consistency criteria is 1815 $m^2\ g^{-1}$, confirming efficient activation.

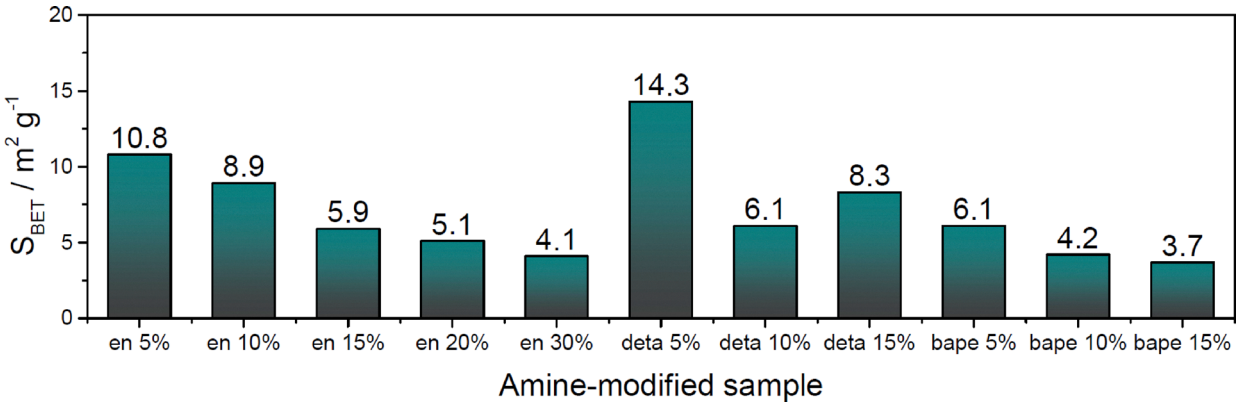

Fig. 5 The comparison of S_{BET} areas for amine-modified materials.

Upon post-synthetic modification with polyamines, a pronounced decrease in accessible surface area was observed for all functionalized samples compared to MOF-14 (AC), consistent with partial pore filling and blockage by amine molecules. The extent of S_{BET} reduction depended on both the type and loading of the amine (Fig. 5 and Table 3). For ethylenediamine, the surface area decreased progressively from 10.8 m^2 g^{-1} at 5 wt% loading to 4.1 m^2 g^{-1} at 30 wt%, reflecting the efficient pore penetration of this small, bidentate amine. In contrast, diethylenetriamine at 5 wt% retained the highest relative surface area among all modified samples (14.3 m^2 g^{-1}), while higher loadings (10 and 15 wt%) led to a pronounced drop (6.1 and 8.3 m^2 g^{-1}, respectively), likely due to steric hindrance and pore blocking by the bulkier tridentate ligand. For 1,2-bis(3-aminopropylamino)ethane, which is the largest tetraamine tested, even low loadings resulted in a marked reduction in surface area (6.1 m^2 g^{-1} at 5 wt%), with further decreases at 10 and 15 wt% (4.2 and 3.7 m^2 g^{-1}, respectively). This trend is attributed to the larger molecular size and greater number of donor atoms, which promote strong coordination to open Cu(II) sites but also substantially reduce accessible pore volume.

The observed decrease in S_{BET} with increasing amine loading reflects the balance between framework functionalization and retention of porosity. While amine grafting introduces polar sites beneficial for CO_2 adsorption and electrochemical activity, excessive loading can compromise gas-accessible surface area, highlighting the need for optimization depending on the intended application.

3.6 Carbon dioxide adsorption measurements

Carbon dioxide adsorption measurements were performed at 0 °C up to 101 325 Pa on pristine MOF-14 and amine-modified materials. Uptakes are reported as $V(CO_2)$ (cm^3 g^{-1}, STP), $n(CO_2)$ (mmol g^{-1}), and $w(CO_2)$ (wt%). The complete results are summarized in Table 3, and representative isotherms are shown in Fig. 6.

The activated MOF-14 displays the highest total CO_2 capacity within the series, reaching 129.7 cm^3 g^{-1} (5.79 mmol g^{-1}; 25.47 wt%) at 0 °C and 101 325 Pa (Fig. 6). This performance is consistent with its very high specific surface area (1815 m^2 g^{-1}) and the presence of accessible coordinatively unsaturated Cu(II) sites that provide strong adsorption centres for CO_2. Incorporation of en decreases the accessible porosity but introduces basic sites that promote CO_2 binding (Fig. 6a). The uptake evolves with loading as 31.8 → 61.2 → 53.7 → 45.6 → 43.1 cm^3 g^{-1} for 5, 10, 15, 20, 30 wt% en, respectively (*i.e.*, 1.42, 2.73, 2.40, 2.03, 1.92 mmol g^{-1}). The maximum around 10–15 wt% reflects a balance between increasing amine site density (favouring chemisorption) and progressive pore blocking at higher loadings. Deta-functionalized samples deliver robust and nearly composition-independent capacities, with 57.5, 57.2, 58.6 cm^3 g^{-1} for 5, 10, 15 wt%, respectively (≈2.55–2.61 mmol g^{-1}) (Fig. 6b). Despite the lower S_{BET} than pristine MOF-14, the higher number of amine functions per molecule sustains strong CO_2 affinity while avoiding excessive pore occlusion within this loading window. The bulkier tetraamine bape causes a monotonic decrease with loading: 50.9, 43.4, 35.1 cm^3 g^{-1} at 5, 10, 15 wt% (*i.e.*, 2.27, 1.94, 1.57 mmol g^{-1}) (Fig. 6c). These trends are consistent with steric hindrance and partial pore blocking, which limit the accessible volume and reduce the net benefit of the higher nominal number of amine groups.

To provide additional insight into adsorption efficiency, the CO_2 uptake was normalized to the BET surface area (expressed as cm^3 CO_2 per m^2, Table 3). Although pristine MOF-14 (AC) exhibits the highest total CO_2 uptake due to its large accessible surface area, its normalized uptake is only 0.07 cm^3 m^{-2}. In contrast, the amine-functionalized samples display substantially higher CO_2 adsorption density per unit surface area, with values ranging from 2.94 to 10.51 cm^3 m^{-2}. In the en series, the normalized uptake increases systematically with amine loading (2.94 → 6.88 → 9.10 cm^3 m^{-2} for 5–15 wt%), reaching a maximum of 10.51 cm^3 m^{-2} at 30 wt% loading. Similar enhancements are observed for the deta and bape series, where values up to ∼9–10 cm^3 m^{-2} are obtained. Overall, this corresponds to an increase of approximately one to two orders of magnitude compared to pristine MOF-14, indicating a transition from predominantly surface-area-driven physisorption in MOF-14 (AC) to functionality-driven adsorption in the amine-modified materials. The markedly higher CO_2 uptake per unit

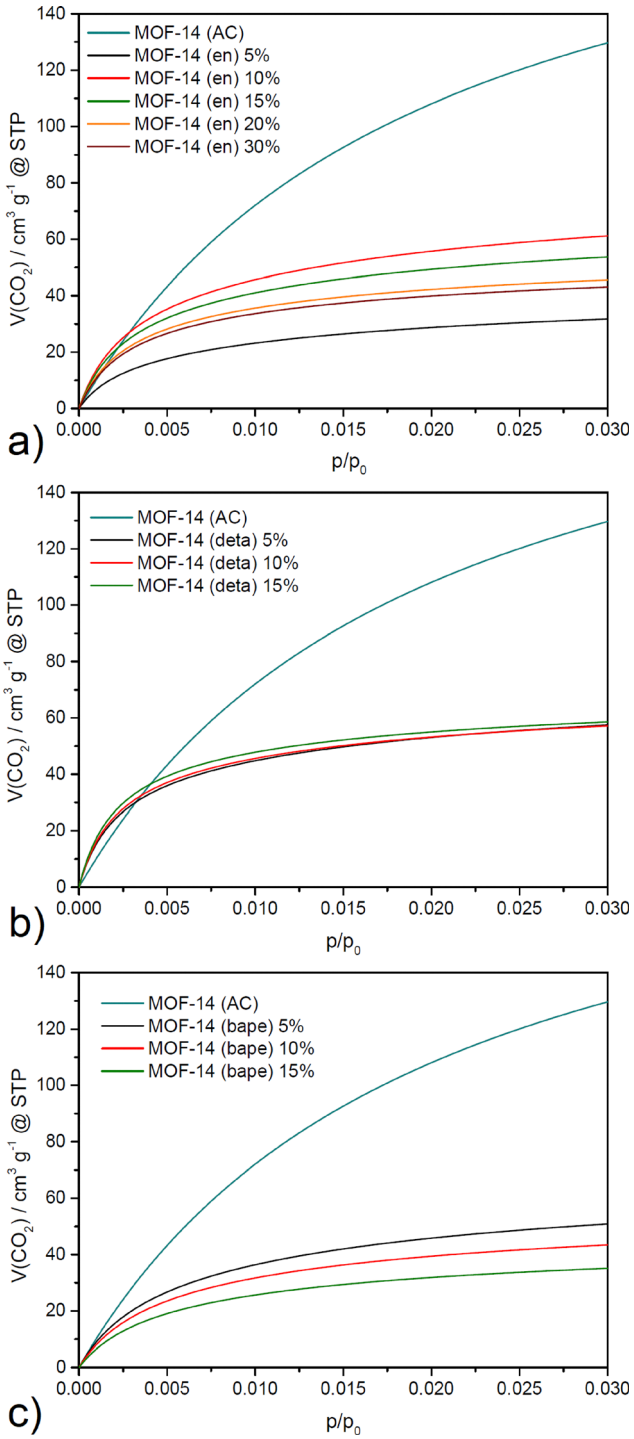

Fig. 6 Comparison of the CO_2 adsorption isotherm of activated MOF-14 and (a) en-, (b) deta- and (c) bape-modified materials with different mass fractions.

N_2-accessible surface area highlights the enhanced adsorption efficiency associated with the introduced amine functionalities.

Fig. 7 shows the relationship between $w(CO_2)$ (wt%) and the real amine content calculated from TG curves (mmol g^{-1}) for MOF-14 modified with en, deta, and bape. For en, a slightly increasing trend is observed with a local maximum at approximately 3.0 mmol g^{-1} (sample MOF-14 (en) 10%, ~12 wt% CO_2), followed by a decline at higher loadings, consistent with pore blocking. The deta series exhibits a nearly constant but slightly positive slope (~11.2–11.5 wt% over 1.6–2.2 mmol g^{-1}), suggesting that multiple –NH groups enhance CO_2 affinity without significantly compromising pore accessibility in this range. In contrast, bape shows a pronounced negative trend, decreasing from ~10 wt% at ~1.9 mmol g^{-1} to ~6.9 wt% at ~2.0 mmol g^{-1}, reflecting steric hindrance and early pore blocking even at moderate loadings. A comparison at similar real amine contents (~1.9–2.0 mmol g^{-1}) indicates the performance order deta > bape > en, with inter-series differences exceeding the variability within each series. Overall, the plot confirms that actual grafted amine content, rather than nominal dosing, is the key predictor of CO_2 uptake, while the amine type critically determines the slope and direction of the trend (positive for en/deta, negative for bape).

While the total capacities at 1 atm for amine-modified samples are lower than for pristine MOF-14, their isotherms exhibit a markedly steeper initial slope (see Fig. 6), evidencing enhanced low-pressure affinity due to CO_2–amine chemisorption superimposed on physisorption. This profile is advantageous in processes operating at sub-atmospheric or modest CO_2 partial pressures, such as post-combustion polishing (VSA/TVSA cycles), indoor/cabin air scrubbing, and personal protective filters, where rapid capture at low $p(CO_2)$ governs performance.[51–53]

Overall, optima near 10–15 wt% (en or deta) maximize low-pressure uptake while limiting pore blocking, offering a complementary alternative to pristine MOF-14, lower total capacity at atmospheric pressure, but superior efficiency in the practically relevant low-pressure regime.

To further evaluate the CO_2 separation performance of the prepared materials under conditions relevant to gas separation processes, additional adsorption measurements were performed for selected representative samples. Four materials were chosen to cover the key structural regimes observed in this study: pristine activated MOF-14 (AC) as the reference material with the highest accessible porosity, MOF-14 (en) 10% representing the composition with the highest CO_2 uptake among the modified samples, MOF-14 (en) 20% corresponding to the material exhibiting the best electrochemical performance (see Section 3.6 Electrochemical measurements below), and MOF-14 (en) 30% representing the high amine loading regime where pore blocking becomes significant. Adsorption isotherms of CO_2 and N_2 at 0 °C were measured for these samples, and the corresponding CO_2/N_2 selectivity values were subsequently calculated. The obtained adsorption capacities and selectivity values are summarized in Table 4.

The adsorption isotherms of CO_2 and N_2 measured at 0 °C are presented in Fig. S7 in SI. The obtained results show that nitrogen adsorption is significantly suppressed in the amine-modified materials. This behaviour can be attributed to partial pore blocking caused by the incorporated amine molecules,

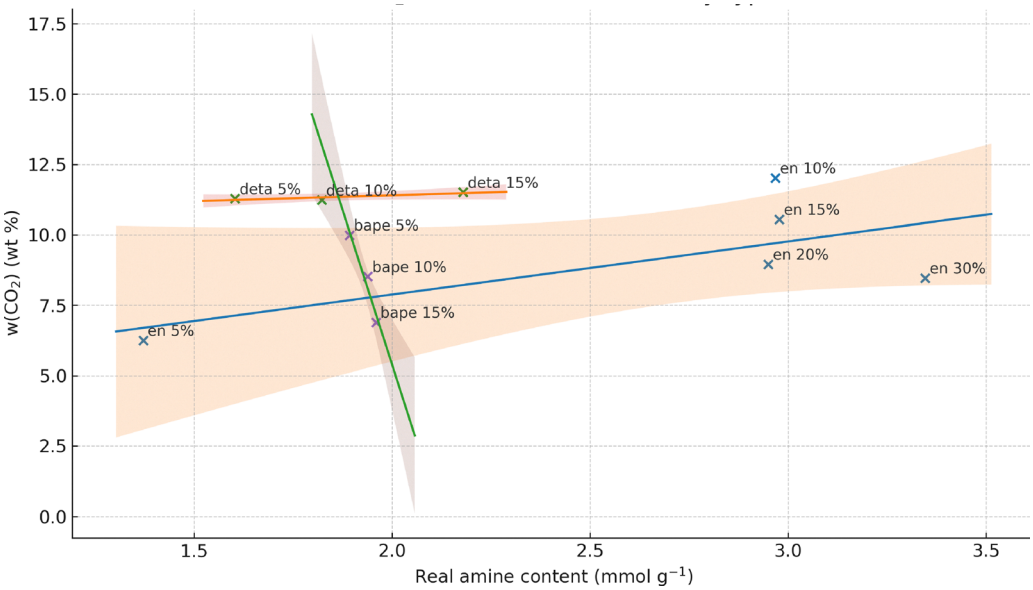

Fig. 7 Correlation between CO_2 uptake (wt%) and real amine content (mmol g^{-1}) for MOF-14 modified with en, deta, and bape.

Table 4 CO_2 and N_2 adsorption capacities@0 °C and 25 °C with calculated CO_2/N_2 selectivity for pristine MOF-14 and selected en-modified samples

Sample	$n(CO_2)$@25 °C (mmol g^{-1})	$n(CO_2)$@0 °C (mmol g^{-1})	$n(N_2)$@0 °C (mmol g^{-1})	Selectivity $n(CO_2)/n(N_2)^a$	SelectivityIAST^b
MOF-14 (AC)	3.24	5.79	0.323	18	105
MOF-14 (en) 10%	1.38	2.73	0.017	161	600
MOF-14 (en) 20%	1.05	2.03	0.011	185	830
MOF-14 (en) 30%	0.97	1.92	0.008	240	880

[a] CO_2/N_2 selectivity at 0 °C was determined from single-component adsorption isotherms as the ratio of the CO_2 uptake to the corresponding N_2 uptake. [b] CO_2/N_2 selectivity calculated for a binary gas mixture containing 15% CO_2 and 85% N_2 using ideal adsorbed solution theory (IAST) based on the fitted single-component adsorption isotherms measured at 0 °C.

which significantly reduces the accessibility of the porous structure for N_2 molecules. In addition, since adsorption is an exothermic process, the adsorbed amount of N_2 further decreases with increasing temperature. Consequently, the selected amine-modified samples adsorb only very small amounts of nitrogen at 0 °C, indicating a strong preference of the framework for CO_2 adsorption.

To quantify this behaviour, CO_2/N_2 selectivity at 0 °C was evaluated using two different approaches. In the first approach, the apparent selectivity was estimated directly from single-component adsorption isotherms as the ratio of the CO_2 uptake to the corresponding N_2 uptake:

$$S_{CO_2/N_2} = \frac{n_{CO_2}}{n_{N_2}}$$

where n_{CO_2} and n_{N_2} represent the adsorbed amounts of CO_2 and N_2 (mmol g^{-1}) at the same pressure (101 325 Pa) and temperature (0 °C). Based on this simple approach, pristine MOF-14 (AC) exhibits a selectivity of 18, while the amine-modified samples show substantially higher values ranging from 161 to 240. The increase in selectivity is primarily associated with the drastic suppression of N_2 adsorption upon amine incorporation.

For comparison, previously reported MOF materials typically exhibit lower CO_2/N_2 selectivities when estimated from single-component adsorption capacities. For example, the widely studied porous framework MIL-101(Cr) shows a CO_2/N_2 selectivity of approximately 7.4 under comparable conditions.[54] Amine-functionalized MOF materials generally exhibit higher selectivity due to stronger interactions between CO_2 molecules and basic amine sites. For instance, the ethylenediamine-functionalized framework ED@MOF-520 shows a CO_2/N_2 selectivity of $\sim$50,[55] while the amine-decorated CAU-1 framework exhibits a selectivity of about 101.[56] In contrast, the amine-modified MOF-14 samples investigated in this work display substantially higher values ranging from 161 to 240, demonstrating the strong preference of the functionalized framework for CO_2 adsorption.

To obtain a more realistic estimate of separation performance under mixed-gas conditions, the selectivity was also evaluated using ideal adsorbed solution theory (IAST).[57] IAST is a thermodynamic model widely used to predict multicomponent adsorption behaviour from single-component adsorption

isotherms. The selectivity for a binary gas mixture can be expressed as:

$$S_{CO_2/N_2} = \frac{x_{CO_2}/x_{N_2}}{y_{CO_2}/y_{N_2}}$$

where x_i represents the mole fraction of component i in the adsorbed phase and y_i represents the mole fraction of the corresponding component in the gas phase. In this work, the selectivity was calculated for a typical post-combustion gas mixture containing 15% CO_2 and 85% N_2. The calculated IAST selectivity values increase from 105 for pristine MOF-14 to values between 600 and 880 for the amine-modified samples (see Table 4).

For comparison, the IAST-predicted CO_2/N_2 selectivity for flue-gas mixtures containing 15% CO_2 and 85% N_2 was compared with previously reported amine-functionalized MOF materials. Amine-tethered MIL-101-DETA exhibits CO_2/N_2 selectivity of 346, demonstrating the beneficial effect of grafted amine functionalities on CO_2 affinity.[58] Comparable values have been reported for diamine-appended frameworks such as dmpn-Mg_2(dobpdc) (dmpn = 2,2-dimethyl-1,3-propanediamine; dobpdc = 4,4′-dioxidobiphenyl-3,3′-dicarboxylate), which display CO_2/N_2 selectivity of approximately 300–400 due to cooperative CO_2 adsorption within the framework channels.[59] Even higher separation performance has been reported for polyethylenimine-modified MIL-101(Cr), reaching CO_2/N_2 selectivity values of 600–770 under flue-gas conditions, depending on the PEI loading within the framework.[60] Among the most extreme examples are diamine-appended frameworks such as mmen-Mg_2(dobpdc) (mmen = *N*,*N*′-dimethylethylenediamine), which exhibit exceptionally high CO_2/N_2 selectivity exceeding 49 000, attributed to cooperative chemisorption of CO_2 forming ammonium carbamate chains within the framework pores.[61]

In comparison with previously reported systems, the amine-modified MOF-14 materials investigated in this work exhibit high IAST CO_2/N_2 selectivity values ranging from 600 to 880. The incorporation of ethylenediamine into the MOF-14 framework, therefore, strongly enhances the preferential adsorption of CO_2 over N_2, placing these materials among highly competitive MOF-based adsorbents reported for CO_2/N_2 separation under flue-gas conditions. Although amine incorporation partially reduces the total CO_2 adsorption capacity due to pore blocking, it significantly improves separation performance by suppressing N_2 adsorption and promoting strong CO_2–amine interactions within the modified framework. Furthermore, immobilization of amine molecules within a solid MOF matrix provides an additional practical advantage, as free amines are typically liquid, highly reactive, and corrosive,[62] whereas their incorporation into the porous framework yields a stable solid adsorbent that is easier to handle and integrate into practical adsorption processes.

Up to this point, the discussion has primarily focused on CO_2 adsorption behaviour at 0 °C, which was used as the reference condition for evaluating adsorption capacities and

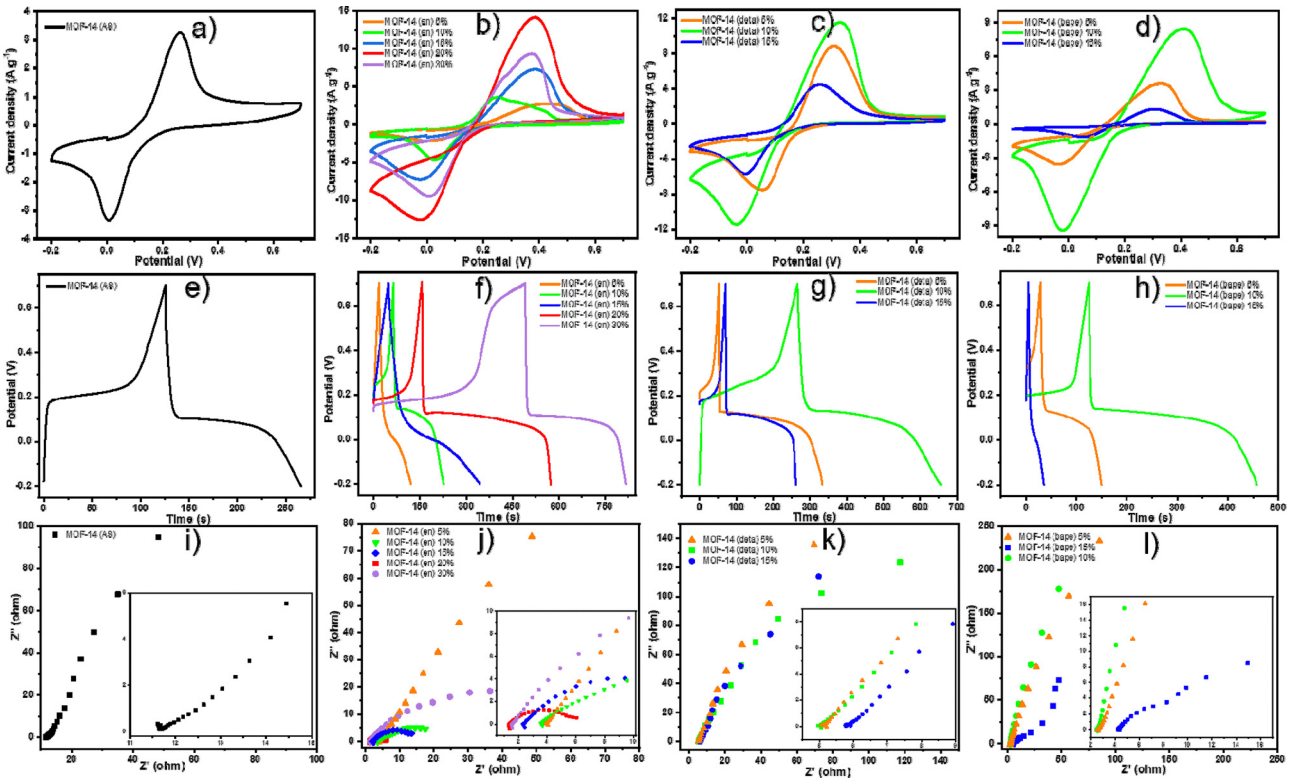

Fig. 8 (a)–(d) CV at 10 mV s^{-1}, (e)–(h) GCD at 1 A g^{-1} and (i)–(l) EIS curve for MOF-14 (AS), MOF-14 (en), MOF-14 (deta) and MOF-14 (bape).

CO_2/N_2 selectivity. In order to assess the adsorption performance under conditions closer to practical gas separation processes, additional adsorption measurements were carried out at 25 °C. The obtained CO_2 capacities at ambient temperature are summarized in Table 4. At 25 °C, the pristine MOF-14 (AC) exhibits a CO_2 uptake of 3.24 mmol g^{-1}, whereas the amine-modified samples display lower adsorption capacities ranging from 0.97 to 1.38 mmol g^{-1}. Among the modified materials, MOF-14 (en) 10% shows the highest uptake (1.38 mmol g^{-1}), indicating that moderate amine loading provides a favourable balance between accessible porosity and the density of CO_2-affinitive amine sites. Further increase in amine content leads to a gradual decrease in CO_2 uptake (1.05 and 0.97 mmol g^{-1} for MOF-14 (en) 20% and 30%, respectively).

3.7 Electrochemical measurements

Electrochemical measurements, including cyclic voltammetry (CV), galvanostatic charge discharge (GCD) and electrochemical impedance spectroscopy (EIS) (see Fig. 8 and Table 5) were performed on a 3-electrode cell using 1 M H_2SO_4 as an electrolyte, Ag/AgCl electrode as reference electrode, and utilizing the platinum wire as counter electrode. For the working electrode, a slurry was prepared by adding synthesized material, acetylene black and binder in an 8 : 1 : 1 ratio in DMF solvent. This solution was sonicated for 2 h, and the obtained slurry was pasted on a high-density graphite sheet with thickness 0.5 mm, using the drop casting technique.[63] The loaded mass evaluated by subtracting the mass of electrode from the mass of electrode pasted with active material was controlled at 1 mg cm^{-2}. Since all electrodes were prepared with a fixed content of acetylene black, any change in the electrochemical performance is attributed to framework functionalization rather than variation in conductive additive content.

Fig. 8(a)–(d) demonstrates the CV curve of MOF-14 (AS), MOF-14 (en), MOF-14 (deta) and MOF-14 (bape) at a scan rate of 10 mV s^{-1} in the potential range from −0.2 V to 0.7 V. The clear appearance of redox peaks in the CV curve shows the presence of redox reactions. The value of peak current increases on modifying the samples with amine, reaching a maximum value of 972.22 F g^{-1} for MOF-14 (en) 20%. This might be attributed to the introduction of polar functional sites due to the amine group, which enhances the material's ability to adsorb and store charge electrostatically. On further increasing the amine concentration beyond a specific value, the peak current and hence the area under the CV curve decrease, which might be due to the blocking of pores because of excessive amine concentration, which impedes the charge transfer process and thus reduces specific capacitance.

The charge-storing ability of MOF-14 samples was further analyzed by performing GCD at a current density of 1 A g^{-1}, as shown in Fig. 8(e)–(h). A non-linear relation between the potential and time in the GCD curve represents the pseudocapacitive charge storage mechanism of material. The shape of modified MOF-14 samples resembles well of the unmodified MOF-14 with an increase in charging and discharging time symbolizing the same charge storage mechanism as MOF-14 (AS). The increase in discharging time in modified MOF-14 can be attributed to additional adsorption sites of the amine group, which contribute to longer charging–discharging time and hence increase the specific capacitance of the material with a maximum value of 465.80 F g^{-1} for MOF-14 (en) 20%. The specific capacitance of the material from CV and GCD is calculated using the following equations.[64,65]

$$C_{CV} = \frac{\int I \mathrm{d}V}{m\nu\Delta V}$$

$$C_{GCD} = \frac{I \times \mathrm{d}t}{m \times \mathrm{d}V}$$

where C_{CV} and C_{GCD} represent the specific capacitance from CV and GCD measurements, $\int I \mathrm{d}V$ represents the area under the CV curve, I, $\mathrm{d}t$, m, ν, and ΔV shows the discharging time, current, mass of material deposited on the electrode, scan rate and potential window, respectively. Table 5 summarizes the specific capacitance evaluated for all the samples from CV and GCD measurements. The highest value of specific capacitance was observed for MOF-14 (en) 20% sample.

Table 5 Value of specific capacitance in three-electrode configuration for as-synthesized and amine-modified MOF-14

Sample	Specific capacitance (F g^{-1})	
	C_{CV}	C_{GCD}
MOF-14 (AS)	180.13	157.10
MOF-14 (en) 5%	186.41	117.87
MOF-14 (en) 10%	232.12	183.54
MOF-14 (en) 15%	470.95	332.19
MOF-14 (en) 20%	972.22	465.80
MOF-14 (en) 30%	758.30	359.09
MOF-14 (deta) 5%	474.41	313.50
MOF-14 (deta) 10%	706.85	432.82
MOF-14 (deta) 15%	302.88	212.03
MOF-14 (bape) 5%	221.93	135.43
MOF-14 (bape) 10%	540.72	368.53
MOF-14 (bape) 15%	71.45	33.44

The effect on conductivity of modified MOF-14 samples was analyzed by obtaining the electrochemical impedance spectroscopy (EIS) in a frequency range from 100 kHz to 0.1 Hz. In the high-frequency region, the absence of a semi-circle in all the samples demonstrates the supercapacitive behavior of the MOF-14 sample. In addition, the beginning of the arc in high frequency region shows the solution resistance, which is minimum for MOF-14 (en) 20%, thus validating the CV and GCD results. In addition, the angled line in a low-frequency region shows the capacitive and diffusive contribution to the specific capacitance. It is concluded that the unmodified or MOF-14 (AS) sample has a capacitive contribution, while its amine modification results in both capacitive and diffusive contributions, resulting in better energy storage performance.

From Table 5, it is evident that among the amine modifications, ethylenediamine (en) modification results in better energy storage properties than deta and bape. This might be due to the optimized balance between pore accessibility and

Table 6 Comparison of specific capacitance of amine-modified MOF-14 with other MOF materials

Material	Specific capacitance (F g^{-1})	Ref.
Cd_AT-BP/rGO	58.5@5 mV s^{-1}	44
Cd_AT-BP/CNT	17.5@5 mV s^{-1}	44
Ammonia functionalized ZIF-8	260@2 A g^{-1}	66
Mn–Ni MOF	711@1 A g^{-1}	67
Covalent graphene-MOF	651@2 A g^{-1}	68
ZnCo-MOF/GS	695@1 A g^{-1}	69
Zn-MOF/PANI	372@0.1 A g^{-1}	70
Ni-Tyr-NDI-MOF/GF	330@1 A g^{-1}	71
rGO/Ni-MOF@PANI	204@0.5 A g^{-1}	72
MOF-14 (en) 20%	972@10 mV s^{-1} 466@1 A g^{-1}	This work

ion diffusion for MOF-14 (en). This ensures the minimum pore blockage and allows the ions to access the high specific surface area of MOF-14, and helps in faster ion transport. For MOF-14 (deta) and MOF-14 (bape), a higher density of amine functional groups results in agglomeration and blocks the pores of MOF-14, thus compromising the electrochemical performance.

These materials were developed as electrode materials in order to accumulate electrochemical energy. For MOF-14 (en) 20%, an excellent specific capacitance value of 972.22 F g^{-1} (from CV) and 465.80 F g^{-1} (from GCD) was observed compared to other investigated MOF materials (see Table 6). The lower GCD value confirms that diffusion limitations are present at constant current conditions, which supports that the reported CV value is not artificially inflated but scan-rate dependent. The synthesized and amine-modified MOF-14 nanocomposites exhibit great potential as an electrode material under three electrode configuration. While the present study focuses on elucidating charge storage characteristics rather than full device optimization, the notable CV and GCD responses suggest that controlled amine modification is an effective strategy for improving electrochemical performance in MOF-based systems. These findings provide a mechanistic foundation for further investigation toward practical supercapacitor configurations and long-term cycling evaluation.

4. Conclusion

In summary, this work demonstrates that post-synthetic amine functionalization provides a versatile and effective route to tailor the performance of MOF-14 for CO_2 capture and electrochemical energy storage. Ethylenediamine, diethylenetriamine, and 1,2-bis(3-aminopropylamino)ethane were successfully introduced into the MOF framework without compromising structural stability; however, the balance between available porosity and functional group density was strongly governed by the amine type and incorporation level. CO_2 adsorption studies revealed that moderate loadings of en and deta (10–15 wt%) afforded the highest uptake, leveraging enhanced chemisorptive interactions while maintaining sufficient pore accessibility, whereas bape induced significant steric restriction. Furthermore, evaluation of CO_2/N_2 separation performance, including both single-component selectivity estimates and IAST calculations for a 15% CO_2/85% N_2 mixture, demonstrated that amine incorporation substantially enhances the preferential adsorption of CO_2 over N_2. The amine-modified MOF-14 materials exhibit high selectivity values, placing them among competitive MOF-based adsorbents for CO_2/N_2 separation under flue-gas conditions. Electrochemical analysis identified MOF-14 (en) 20% as a high-performing electrode material, delivering a remarkable specific capacitance of 972 F g^{-1}, significantly exceeding that of the pristine parent material.

Overall, the results highlight the critical role of optimizing functional group incorporation to achieve multifunctionality within a single material system. Importantly, controlled amine loading enables rational tuning of MOF-14 toward either optimized CO_2 capture or enhanced electrochemical energy storage, underscoring its adaptability as a multifunctional materials platform rather than reliance on a single universally optimal composition. By judicious adjustment of amine content, MOF-14 can therefore be selectively tailored depending on the targeted application. This study positions amine-modified MOF-14 as a promising platform for next-generation applications at the intersection of environmental remediation and energy storage technologies.

Conflicts of interest

There are no conflicts to declare.

Data availability

The data supporting this article have been included in the manuscript itself and as part of the supplementary information (SI). Supplementary information includes additional characterization data such as PXRD, IR spectra, TG/DTA analysis, EDX data, and gas adsorption measurements (N_2 and CO_2), along with images of the prepared samples. See DOI: https://doi.org/10.1039/d5ma01438g.

The raw data will also be made available upon genuine request.

Acknowledgements

P. S. gratefully acknowledges the financial support of the Department of Science and Technology, Ministry of Science and Technology, Govt. of India, for women scientists under WISE-PhD grant (DST/WISE-PhD/PM/2023/110). Manisha gratefully acknowledge the Council of Scientific and Industrial Research (CSIR) for awarding the Senior Research Fellowship (Ref. No. 16/06/2019(i) EU-V). AS is highly thankful to Science and Engineering Board (SERB), Department of Science and Technology (DST), Government of India for providing research funding under the SERB Startup Research Grant (SRG) scheme (File No. SRG/2021/002019) and SERB International Research Experience (SIRE) scheme (File No. SIR/2022/001589). M. A. thanks EU NextGenerationEU through the

Recovery and Resilience Plan for Slovakia under the project no. 09I03-03-V03-00034 (MASS-PRAM), no. 09I02-03-V01-00022 (SUNFLOWERS), VEGA project no. 1/0058/25, and the European Union for providing a grant under KA171 – Mobility of higher education students and staff call. The authors thank Klaudia Simanova from Pavol Jozef Safarik University in Kosice, Slovak Republic, for the preparation of the materials.

References

1 M. Ding, X. Cai and H.-L. Jiang, Improving MOF stability: approaches and applications, *Chem. Sci.*, 2019, **10**, 10209–10230, DOI: 10.1039/C9SC03916C.

2 R. Freund, O. Zaremba, G. Arnauts, R. Ameloot, G. Skorupskii, M. Dincă, A. Bavykina, J. Gascon, A. Ejsmont, J. Goscianska, M. Kalmutzki, U. Lächelt, E. Ploetz, C. S. Diercks and S. Wuttke, The Current Status of MOF and COF Applications, *Angew. Chem., Int. Ed.*, 2021, **60**, 23975–24001, DOI: 10.1002/anie.202106259.

3 T. Zelenka, M. Baláž, M. Férová, P. Diko, J. Bednarčík, A. Királyová, Ľ. Zauška, R. Bureš, P. Sharda, N. Király, A. Badač, J. Vyhlídalová, M. Želinská and M. Almáši, The influence of HKUST-1 and MOF-76 hand grinding/mechanical activation on stability, particle size, textural properties and carbon dioxide sorption, *Sci. Rep.*, 2024, **14**, 15386, DOI: 10.1038/s41598-024-66432-z.

4 A. R. Yuvaraj, A. Jayarama, D. Sharma, S. S. Nagarkar, S. P. Duttagupta and R. Pinto, Role of metal-organic framework in hydrogen gas storage: A critical review, *Int. J. Hydrogen Energy*, 2024, **59**, 1434–1458, DOI: 10.1016/j.ijhydene.2024.02.060.

5 P. Wang, Y. Teng, J. Zhu, W. Bao, S. Han, Y. Li, Y. Zhao and H. Xie, Review on the synergistic effect between metal–organic frameworks and gas hydrates for CH4 storage and CO2 separation applications, *Renewable Sustainable Energy Rev.*, 2022, **167**, 112807, DOI: 10.1016/j.rser.2022.112807.

6 Y. Shen, T. Pan, L. Wang, Z. Ren, W. Zhang and F. Huo, Programmable Logic in Metal–Organic Frameworks for Catalysis, *Adv. Mater.*, 2021, **33**(46), 2007442, DOI: 10.1002/adma.202007442.

7 J. Liu, T. A. Goetjen, Q. Wang, J. G. Knapp, M. C. Wasson, Y. Yang, Z. H. Syed, M. Delferro, J. M. Notestein, O. K. Farha and J. T. Hupp, MOF-enabled confinement and related effects for chemical catalyst presentation and utilization, *Chem. Soc. Rev.*, 2022, **51**, 1045–1097, DOI: 10.1039/D1CS00968K.

8 S. Mallakpour, E. Nikkhoo and C. M. Hussain, Application of MOF materials as drug delivery systems for cancer therapy and dermal treatment, *Coord. Chem. Rev.*, 2022, **451**, 214262, DOI: 10.1016/j.ccr.2021.214262.

9 M. Almáši, A review on state of art and perspectives of Metal-Organic frameworks (MOFs) in the fight against coronavirus SARS-CoV-2, *J. Coord. Chem.*, 2021, **74**, 2111–2127, DOI: 10.1080/00958972.2021.1965130.

10 V. Huntošová, A. Benziane, L. Zauška, L. Ambro, S. Olejárová, J. Joniová, N. Hlávková, G. Wagnières, G. Zelenková, P. Diko, J. Bednarčík, F. Zákány, T. Kovács, E. Sedlák, G. Vámosi and M. Almáši, The potential of metal–organic framework MIL-101(Al)–NH2 in the forefront of antiviral protection of cells via interaction with SARS-CoV-2 spike RBD protein and their antibacterial action mediated with hypericin and photodynamic treatment, *J. Colloid Interface Sci.*, 2025, **691**, 137454, DOI: 10.1016/j.jcis.2025.137454.

11 Y. Shen, A. Tissot and C. Serre, Recent progress on MOF-based optical sensors for VOC sensing, *Chem. Sci.*, 2022, **13**, 13978–14007, DOI: 10.1039/D2SC04314A.

12 A. Garg, M. Almáši, R. Saini, D. R. Paul, A. Sharma, A. Jain and I. P. Jain, A highly stable terbium(III) metal-organic framework MOF-76(Tb) for hydrogen storage and humidity sensing, *Environ. Sci. Pollut. Res.*, 2022, **30**, 98548–98562, DOI: 10.1007/s11356-022-21290-y.

13 M. Almáši, A. Sharma and T. Zelenka, Anionic zinc(II) metal-organic framework post-synthetically modified by alkali-ion exchange: Synthesis, characterization and hydrogen adsorption properties, *Inorg. Chim. Acta*, 2021, **526**, 120505, DOI: 10.1016/j.ica.2021.120505.

14 H. Li, X. Li, J. Dai and S. Zheng, Ion exchange in metal-organic frameworks and their derivatives: a facile strategy for enhanced water splitting, *Mater. Today Energy*, 2024, **44**, 101595, DOI: 10.1016/j.mtener.2024.101595.

15 Ľ. Zauška, P. Pillárová, D. Volavka, E. Kinnertová, J. Bednarčík, J. Brus, V. Hornebecq and M. Almáši, Kinetic adsorption mechanism of cobalt(II) ions and Congo red on pristine and Schiff base-surface-modified MIL-101(Fe)-NH2, *Microporous Mesoporous Mater.*, 2025, **386**, 113493, DOI: 10.1016/j.micromeso.2025.113493.

16 N. Király, D. Capková, R. Gyepes, N. Vargová, T. Kazda, J. Bednarčík, D. Yudina, T. Zelenka, P. Čudek, V. Zeleňák, A. Sharma, V. Meynen, V. Hornebecq, A. Straková Fedorková and M. Almáši, Sr(II) and Ba(II) Alkaline Earth Metal–Organic Frameworks (AE-MOFs) for Selective Gas Adsorption, Energy Storage, and Environmental Application, *Nanomaterials*, 2023, **13**, 234, DOI: 10.3390/nano13020234.

17 Y. Sun, N. Zhang, Y. Yue, J. Xiao, X. Huang and A. Ishag, Recent advances in the application of zeolitic imidazolate frameworks (ZIFs) in environmental remediation: a review, *Environ. Sci.: Nano*, 2022, **9**, 4069–4092, DOI: 10.1039/D2EN00601D.

18 H. Musarurwa and N. T. Tavengwa, Smart metal-organic framework (MOF) composites and their applications in environmental remediation, *Mater. Today Commun.*, 2022, **33**, 104823, DOI: 10.1016/j.mtcomm.2022.104823.

19 V. Niščáková, M. Almáši, D. Capková, T. Kazda, O. Čech, P. Čudek, O. Petruš, D. Volavka, R. Oriňaková and A. S. Fedorková, Novel Cu(II)-based metal–organic framework STAM-1 as a sulfur host for Li–S batteries, *Sci. Rep.*, 2024, **14**, 9232, DOI: 10.1038/s41598-024-59600-8.

20 Y. Peng, J. Xu, J. Xu, J. Ma, Y. Bai, S. Cao, S. Zhang and H. Pang, Metal-organic framework (MOF) composites as promising materials for energy storage applications, *Adv. Colloid Interface Sci.*, 2022, **307**, 102732, DOI: 10.1016/j.cis.2022.102732.

21 R. Du, Y. Wu, Y. Yang, T. Zhai, T. Zhou, Q. Shang, L. Zhu, C. Shang and Z. Guo, Porosity Engineering of MOF-Based Materials for Electrochemical Energy Storage, *Adv. Energy Mater.*, 2021, **11**(20), 2100154, DOI: 10.1002/aenm.202100154.

22 C. Pettinari and A. Tombesi, Metal–organic frameworks for carbon dioxide capture, *MRS Energy Sustainability*, 2020, **7**, 35, DOI: 10.1557/mre.2020.30.

23 M. Ding, R. W. Flaig, H.-L. Jiang and O. M. Yaghi, Carbon capture and conversion using metal–organic frameworks and MOF-based materials, *Chem. Soc. Rev.*, 2019, **48**, 2783–2828, DOI: 10.1039/C8CS00829A.

24 V. Irani, A. Tavasoli, A. Maleki and M. Vahidi, Polyethyleneimine-functionalized HKUST-1/MDEA nanofluid to enhance the absorption of CO2 in gas sweetening process, *Int. J. Hydrogen Energy*, 2018, **43**, 5610–5619, DOI: 10.1016/j.ijhydene.2018.01.120.

25 S. Gaikwad, Y. Kim, R. Gaikwad and S. Han, Enhanced CO2 capture capacity of amine-functionalized MOF-177 metal organic framework, *J. Environ. Chem. Eng.*, 2021, **9**, 105523, DOI: 10.1016/j.jece.2021.105523.

26 A. Justin, J. Espín, M. J. Pougin, D. Stoian, T. Schertenleib, M. Mensi, I. Kochetygov, A. Ortega-Guerrero and W. L. Queen, Post-Synthetic Covalent Grafting of Amines to NH_2-MOF for Post-Combustion Carbon Capture, *Adv. Funct. Mater.*, 2024, **34**(7), 2307430, DOI: 10.1002/adfm.202307430.

27 T. S. Nguyen, N. A. Dogan, H. Lim and C. T. Yavuz, Amine Chemistry of Porous CO_2 Adsorbents, *Acc. Chem. Res.*, 2023, **56**, 2642–2652, DOI: 10.1021/acs.accounts.3c00367.

28 A. Sarkar, A. K. Jana and S. Natarajan, Aliphatic amine mediated assembly of $[M_6(mna)_6]$ (M = Cu/Ag) into extended two-dimensional structures: synthesis, structure and Lewis acid catalytic studies, *New J. Chem.*, 2021, **45**, 6503–6511, DOI: 10.1039/D1NJ00544H.

29 S. Mutyala, M. Jonnalagadda, H. Mitta and R. Gundeboyina, CO2 capture and adsorption kinetic study of amine-modified MIL-101 (Cr), *Chem. Eng. Res. Des.*, 2019, **143**, 241–248, DOI: 10.1016/j.cherd.2019.01.020.

30 M. Ding, W. Rong, Y. Wang, S. Kong and J. Yao, Pore engineering of metal–organic frameworks for boosting low-pressure CO_2 capture, *J. Mater. Chem. A*, 2023, **11**, 25784–25802, DOI: 10.1039/D3TA05413F.

31 S. Ye, X. Jiang, L.-W. Ruan, B. Liu, Y.-M. Wang, J.-F. Zhu and L.-G. Qiu, Post-combustion CO2 capture with the HKUST-1 and MIL-101(Cr) metal–organic frameworks: Adsorption, separation and regeneration investigations, *Microporous Mesoporous Mater.*, 2013, **179**, 191–197, DOI: 10.1016/j.micromeso.2013.06.007.

32 G. Chakraborty, P. Das and S. K. Mandal, Efficient and Highly Selective CO $_2$ Capture, Separation, and Chemical Conversion under Ambient Conditions by a Polar-Group-Appended Copper(II) Metal–Organic Framework, *Inorg. Chem.*, 2021, **60**, 5071–5080, DOI: 10.1021/acs.inorgchem.1c00101.

33 J. H. Choe, H. Kim, H. Yun, J. F. Kurisingal, N. Kim, D. Lee, Y. H. Lee and C. S. Hong, Extended MOF-74-Type Variant with an Azine Linkage: Efficient Direct Air Capture and One-Pot Synthesis, *J. Am. Chem. Soc.*, 2024, **146**, 19337–19349, DOI: 10.1021/jacs.4c05318.

34 H. Woo, A. M. Devlin and A. J. Matzger, In Situ Observation of Solvent Exchange Kinetics in a MOF with Coordinatively Unsaturated Sites, *J. Am. Chem. Soc.*, 2023, **145**, 18634–18641, DOI: 10.1021/jacs.3c06396.

35 Ü. Kökçam-Demir, A. Goldman, L. Esrafili, M. Gharib, A. Morsali, O. Weingart and C. Janiak, Coordinatively unsaturated metal sites (open metal sites) in metal–organic frameworks: design and applications, *Chem. Soc. Rev.*, 2020, **49**, 2751–2798, DOI: 10.1039/C9CS00609E.

36 A. A. Olajire, Synthesis chemistry of metal-organic frameworks for CO 2 capture and conversion for sustainable energy future, *Renewable Sustainable Energy Rev.*, 2018, **92**, 570–607, DOI: 10.1016/j.rser.2018.04.073.

37 Z. Hu, Y. Wang, B. B. Shah and D. Zhao, CO_2 Capture in Metal–Organic Framework Adsorbents: An Engineering Perspective, *Adv. Sustainable Syst.*, 2019, **3**(1), 1800080, DOI: 10.1002/adsu.201800080.

38 C. A. Trickett, A. Helal, B. A. Al-Maythalony, Z. H. Yamani, K. E. Cordova and O. M. Yaghi, The chemistry of metal–organic frameworks for CO2 capture, regeneration and conversion, *Nat. Rev. Mater.*, 2017, **2**, 17045, DOI: 10.1038/natrevmats.2017.45.

39 J. Liang and K. Liang, Nano-bio-interface engineering of metal-organic frameworks, *Nano Today*, 2021, **40**, 101256, DOI: 10.1016/j.nantod.2021.101256.

40 V. D. C. Cotlame-Salinas, A. López-Olvera, A. Islas-Jácome, E. González-Zamora and I. A. Ibarra, CO_2 capture enhancement in MOFs *via* the confinement of molecules, *React. Chem. Eng.*, 2021, **6**, 441–453, DOI: 10.1039/D0RE00410C.

41 S. Mandal, S. Natarajan, P. Mani and A. Pankajakshan, Post-Synthetic Modification of Metal–Organic Frameworks Toward Applications, *Adv. Funct. Mater.*, 2021, **31**(4), 2006291, DOI: 10.1002/adfm.202006291.

42 R. Bhosale, S. Bhosale, P. Kumbhar, D. Narale, R. Ghaware, C. Jambhale and S. Kolekar, Design and development of a porous nanorod-based nickel-metal–organic framework (Ni-MOF) for high-performance supercapacitor application, *New J. Chem.*, 2023, **47**, 6749–6758, DOI: 10.1039/D3NJ00456B.

43 S. Krishnan, A. K. Gupta, M. K. Singh, N. Guha and D. K. Rai, Nitrogen-rich Cu-MOF decorated on reduced graphene oxide nanosheets for hybrid supercapacitor applications with enhanced cycling stability, *Chem. Eng. J.*, 2022, **435**, 135042, DOI: 10.1016/j.cej.2022.135042.

44 S. Khan, A. R. Lone, M. Y. Khan, S. Rahaman, K. Pandey, A. Helal, F. Sama and M. Shahid, Engineered Amine-Functionalized Metal–Organic Framework to Fabricate a Composite for Next-Generation Asymmetric Supercapacitors with Ultrahigh Performance: Modulating the Energy Storage Barrier, *Langmuir*, 2024, **40**, 21106–21119, DOI: 10.1021/acs.langmuir.4c02522.

45 Y. Wu, V. K. Peterson, E. Luks, T. A. Darwish and C. J. Kepert, Interpenetration as a Mechanism for Negative

Thermal Expansion in the Metal–Organic Framework $Cu_3(btb)_2$ (MOF-14), *Angew. Chem., Int. Ed.*, 2014, **53**, 5175–5178, DOI: 10.1002/anie.201311055.

46 T. Zelenka, K. Simanova, R. Saini, G. Zelenkova, S. P. Nehra, A. Sharma and M. Almasi, Carbon dioxide and hydrogen adsorption study on surface-modified HKUST-1 with diamine/triamine, *Sci. Rep.*, 2022, **12**, 17366, DOI: 10.1038/s41598-022-22273-2.

47 B. Chen, M. Eddaoudi, S. T. Hyde, M. O'Keeffe and O. M. Yaghi, Interwoven Metal-Organic Framework on a Periodic Minimal Surface with Extra-Large Pores, *Science*, 2001, **291**, 1021–1023, DOI: 10.1126/science.1056598.

48 Ľ. Zauška, E. Beňová, M. Urbanová, J. Brus, V. Zeleňák, V. Hornebecq and M. Almáši, Adsorption and Release Properties of Drug Delivery System Naproxen-SBA-15: Effect of Surface Polarity, Sodium/Acid Drug Form and pH, *J. Funct. Biomater.*, 2022, **13**, 275, DOI: 10.3390/jfb13040275.

49 Ľ. Zauška, T. Zelenka, M. Lisnichuk, P. Pillárová, V. Kuchárová, J. Bednarčík, M. Vilková, S. P. Nehra, A. Sharma, V. Zeleňák, V. Hornebecq and M. Almáši, PEI-Schiff base-modified mesoporous silica materials SBA-12, 15 and 16 for toxic metal ions capture (Co(II), Ni(II) and Cu(II)): Effect of morphology, post-synthetic modification and kinetic study, *Mater. Today Commun.*, 2023, **35**, 106049, DOI: 10.1016/j.mtcomm.2023.106049.

50 M. Thommes, K. Kaneko, A. V. Neimark, J. P. Olivier, F. Rodriguez-Reinoso, J. Rouquerol and K. S. W. Sing, Physisorption of gases, with special reference to the evaluation of surface area and pore size distribution (IUPAC Technical Report, *Pure Appl. Chem.*, 2015, **87**, 1051–1069, DOI: 10.1515/pac-2014-1117.

51 J. Hack, N. Maeda and D. M. Meier, Review on CO_2 Capture Using Amine-Functionalized Materials, *ACS Omega*, 2022, **7**, 39520–39530, DOI: 10.1021/acsomega.2c03385.

52 T. M. McDonald, J. A. Mason, X. Kong, E. D. Bloch, D. Gygi, A. Dani, V. Crocellà, F. Giordanino, S. O. Odoh, W. S. Drisdell, B. Vlaisavljevich, A. L. Dzubak, R. Poloni, S. K. Schnell, N. Planas, K. Lee, T. Pascal, L. F. Wan, D. Prendergast, J. B. Neaton, B. Smit, J. B. Kortright, L. Gagliardi, S. Bordiga, J. A. Reimer and J. R. Long, Cooperative insertion of CO2 in diamine-appended metal-organic frameworks, *Nature*, 2015, **519**, 303–308, DOI: 10.1038/nature14327.

53 M. Åhlén, O. Cheung and C. Xu, Low-concentration CO_2 capture using metal–organic frameworks – current status and future perspectives, *Dalton. Trans.*, 2023, **52**, 1841–1856, DOI: 10.1039/D2DT04088C.

54 D. Jiang, A. D. Burrows and K. J. Edler, Size-controlled synthesis of MIL-101(Cr) nanoparticles with enhanced selectivity for CO2 over N2, *CrystEngComm*, 2011, **13**, 6916, DOI: 10.1039/c1ce06274c.

55 Y. Wan, Y. Miao, R. Zhong and R. Zou, High-Selective CO2 Capture in Amine-Decorated Al-MOFs, *Nanomaterials*, 2022, **12**, 4056, DOI: 10.3390/nano12224056.

56 X. Si, C. Jiao, F. Li, J. Zhang, S. Wang, S. Liu, Z. Li, L. Sun, F. Xu, Z. Gabelica and C. Schick, High and selective CO2 uptake, H2 storage and methanol sensing on the amine-decorated 12-connected MOF CAU-1, *Energy Environ. Sci.*, 2011, **4**, 4522, DOI: 10.1039/c1ee01380g.

57 C. M. Simon, B. Smit and M. Haranczyk, pyIAST: Ideal adsorbed solution theory (IAST) Python package, *Comput. Phys. Commun.*, 2016, **200**, 364–380, DOI: 10.1016/j.cpc.2015.11.016.

58 Y. Hu, W. M. Verdegaal, S. Yu and H. Jiang, Alkylamine-Tethered Stable Metal–Organic Framework for CO_2 Capture from Flue Gas, *ChemSusChem*, 2014, **7**, 734–737, DOI: 10.1002/cssc.201301163.

59 R. L. Siegelman, T. M. McDonald, M. I. Gonzalez, J. D. Martell, P. J. Milner, J. A. Mason, A. H. Berger, A. S. Bhown and J. R. Long, Controlling Cooperative CO_2 Adsorption in Diamine-Appended Mg_2 (dobpdc) Metal–Organic Frameworks, *J. Am. Chem. Soc.*, 2017, **139**, 10526–10538, DOI: 10.1021/jacs.7b05858.

60 Y. Lin, Q. Yan, C. Kong and L. Chen, Polyethyleneimine Incorporated Metal-Organic Frameworks Adsorbent for Highly Selective CO2 Capture, *Sci. Rep.*, 2013, **3**, 1859, DOI: 10.1038/srep01859.

61 T. M. McDonald, W. R. Lee, J. A. Mason, B. M. Wiers, C. S. Hong and J. R. Long, Capture of Carbon Dioxide from Air and Flue Gas in the Alkylamine-Appended Metal–Organic Framework mmen-Mg_2 (dobpdc), *J. Am. Chem. Soc.*, 2012, **134**, 7056–7065, DOI: 10.1021/ja300034j.

62 J. Chang, K. Chen, J. Li, L. Lin, E. Hu, K. Liu and J. Jiang, Liquid amine-based CO2 capture: A review of absorbent systems innovation, multi-scenario applications, and machine learning-assisted optimization, *Renewable Sustainable Energy Rev.*, 2026, **231**, 116754, DOI: 10.1016/j.rser.2026.116754.

63 Manisha, M. T. Qaeemy, M. Dhanda, S. Lata, H. Kumar and A. Sharma, Optimization of Nb2O5/g-C3N4/PPy as an electrode material for prevailing electrochemical performance, *Front. Energy Res.*, 2025, **13**, 1511271, DOI: 10.3389/fenrg.2025.1511271.

64 Manisha, M. Dhanda, R. Arora, A. S. Reddy, S. Lata and A. Sharma, Coalescing of lanthanum oxide and PPy @graphitic carbon nitride to achieve ultrahigh energy density electrode material for supercapacitors applications, *J. Alloys Compd.*, 2023, **955**, 169738, DOI: 10.1016/j.jallcom.2023.169738.

65 Manisha, M. Dhanda, V. Panwar, S. Lata, H. Kumar and A. Sharma, Exploring the effect of magnesium oxide on electrochemical properties of polypyrrole encapsulated on graphitic carbon nitride for supercapacitors applications, *J. Energy Storage*, 2025, **106**, 114698, DOI: 10.1016/j.est.2024.114698.

66 M. Moradi, M. Mousavi, M. Pooriraj, M. Babamoradi and S. Hajati, Enhanced pseudocapacitive performance of two-dimensional Zn-metal organic framework through a post-synthetic amine functionalization, *Thin Solid Films*, 2022, **749**, 139187, DOI: 10.1016/j.tsf.2022.139187.

67 S. Rajasekaran, B. S. Reghunath, K. R. Sunaja Devi, B. Saravanakumar, J. Johnson William, D. Pinheiro and M. K. Arumugam, Facile synthesis of Mn-Ni bimetal organic framework decorated with amine as an electrode for a

high-performance supercapacitor, *J. Solid State Electrochem.*, 2023, **27**, 911–925, DOI: 10.1007/s10008-023-05382-4.

68 K. Jayaramulu, M. Horn, A. Schneemann, H. Saini, A. Bakandritsos, V. Ranc, M. Petr, V. Stavila, C. Narayana, B. Scheibe, Š. Kment, M. Otyepka, N. Motta, D. Dubal, R. Zbořil and R. A. Fischer, Covalent Graphene-MOF Hybrids for High-Performance Asymmetric Supercapacitors, *Adv. Mater.*, 2021, **33**(4), 2004560, DOI: 10.1002/adma.202004560.

69 E. Erçarıkcı, K. Dağcı Kıranşan and E. Topçu, Three-Dimensional ZnCo-MOF Modified Graphene Sponge: Flexible Electrode Material for Symmetric Supercapacitor, *Energy Fuels*, 2022, **36**, 1735–1745, DOI: 10.1021/acs.energyfuels.1c04183.

70 L. Quoc Bao, T.-H. Nguyen, H. Fei, I. Sapurina, F. A. Ngwabebhoh, C. Bubulinca, L. Munster, E. D. Bergerová, A. Lengalova, H. Jiang, T. Trong Dao, N. Bugarova, M. Omastova, N. E. Kazantseva and P. Saha, Electrochemical performance of composites made of rGO with Zn-MOF and PANI as electrodes for supercapacitors, *Electrochim. Acta*, 2021, **367**, 137563, DOI: 10.1016/j.electacta.2020.137563.

71 S. D. Jagadale, S. V. Bhosale and S. V. Bhosale, Nickel Metal–Organic Frameworks of Amino Acid Tyrosine-Functionalized Naphthalenediimide for Pseudocapacitor Applications, *ACS Appl. Eng. Mater.*, 2024, **2**, 1922–1934, DOI: 10.1021/acsaenm.4c00313.

72 N. Q. Khuyen, R. Kiefer and Q. B. Le, rGO/Ni-MOF Composite Modified with PANI Applied as Electrode Materials for Supercapacitor, *Chem. Lett.*, 2023, **52**, 17–21, DOI: 10.1246/cl.220436.